Thermal Photoemitter and Absorber

by Hilma Holmström

Lund
University

Division of Solid State Physics and NanoLund

Thesis for the degree of
Master of Science in Engineering Physics

Supervisor: Ville Maisi
Co-supervisor: Andrea Cicovic

Examiner: Carina Fasth

May 29, 2026

Abstract

The development of controllable thermal photon sources is essential for the advancement of quantum computers, specifically for the development of sensitive detectors and the study of heat transport in superconducting circuits. This thesis investigates a device featuring a metallic copper island acting as a variable thermal bath, coupled to a superconducting microwave line through a clean interface. The device utilizes four adjoining Normal-Insulator-Superconductor (NIS) junctions, enabling both the heating of the island and precise measurements of its electronic temperature. Experimental results demonstrate microwave signal absorption efficiency near 100% and thermal emission reaching close to the theoretical unity limit, thus giving a direct measurement of quantum limited photonic heat conduction. In addition to the emission measurements, this thesis considers the heat flow away from the island. Interestingly, measurements reveal an enhanced heat flux from the island compared to similar previously studied devices, suggesting that specific geometrical parameters may play a critical role in the heat conduction. These findings establish the device as a highly efficient, controllable thermal photon source.

Populärvetenskaplig sammanfattning

Emission och absorption av termiskt ljus på fotonnivå

Vi visar att emission och absorption av mikrovågsfotoner från en nanostruktur i millikelvinområdet når nära 100% effektivitet. Strukturen kan fungera som en termisk fotonkälla för kvantteknologin.

De senaste åren har kvantteknologi vuxit fram som ett nytt spännande forskningsfält som det just nu satsas stora resurser på, både i Sverige och internationellt. Ett av målen med forskningen är att bygga en kvantdator, som skulle kunna utföra vissa typer av komplexa beräkningar på bråkdelen av den tid som det idag tar för en vanlig dator. Istället för bitar i en vanlig dator, som antingen kan ha värdet 0 eller 1, använder kvantdatorer kvantbitar som kan vara både 0 och 1 samtidigt. Flera lovande implementationer av sådana kvantbitar använder sig av mikrovågsfotoner för kommunikation och avläsning av information från beräkningarna. Problemet är att diskreta energipaket av ljus, som mikrovågsfotonerna utgör, har mycket mindre energi än synligt ljus. Därför krävs känsliga och avancerade detektorer för att kunna detektera dessa fotoner.

På fotonnivå beter sig ljus annorlunda beroende på hur det har skapats. Detta analyseras ofta genom fotonstatistik, och går ut på att avgöra hur och med vilket tidsintervall fotoner anländer till en detektor. Det finns tre typer av ljus på fotonnivå, och en avancerad detektor behöver kunna skilja på och avgöra vilken typ som detekteras. Detta kräver förstås en välfungerande fotonkälla, som kan emittera fotoner med en specifik fotonstatistik. Det här arbetet undersöker emissionen från en sådan fotonkälla, som sänder ut termiska fotoner. Termiska fotoner är ljus som har sitt ursprung från värme, och har en specifik statistik som innebär att fotonerna tenderar att emitteras i klungor.

Termiskt ljus är inget unikt för stjärnor eller glödlampor - det finns tvärtom överallt runt oss där det finns värme. I det här sammanhanget behöver dock inte värme vara en temperatur som för oss upplevs varmt, utan termiska fotoner emitteras från alla objekt som har en temperatur över den absoluta nollpunkten. Vilka våglängder som de emitterade fotonerna har beror dock på temperaturen. Det är därför vi kan se ljuset från en stjärna eller glödlampa men inte ljuset från ett objekt i rumstemperatur, eftersom detta objekt inte har tillräckligt mycket värmeenergi för att kunna emittera fotoner med en våglängd i det synliga spektrat.

I det här arbetet undersöks absorptionen och emissionen av termiska mikrovågsfotoner från en liten remsa koppar på nanoskala vid temperaturer mellan 35-500 millikelvin. Vid så här extremt låga temperaturer - bara några tusendelar av en grad ovanför den absoluta nollpunkten - blir emissionen av termiska fotoner en viktig orsak till värmespridning mellan kopparremsan och dess omgivning. Vid rumstemperatur så sprids värme främst genom att fria elektroner rör sig eller genom att atomerna i materialet vibrerar. Men när ett system kyls ner till millikelvinområdet fryser dessa traditionella värmeledningsmekanismer i stort sett fast. Istället transporteras energin genom ett utbyte av termiska fotoner. Genom att mäta emissionen av termiska mikrovågsfotoner kan vi därför också direkt mäta energin från fotonisk värmeledning.

Våra mätningar visar att vi kan uppnå nära perfekt absorption och emission av fotoner. Den uppmätta emissionen av termiska fotoner som funktion av temperatur överenstämmer därför med den teoretiskt maximalt möjliga värmeledningen via fotoner. Även om den fotoniska värmeledningen mellan strukturer har mätts tidigare, utgör det här den första direkta mätningen. Resultaten visar att strukturen fungerar bra som en effektiv och kontrollerbar emitterare av termiska fotoner.

Acknowledgments

First, I would like to extend a big thank you to my supervisors, Ville and Andrea, for your guidance and support throughout this thesis. Ville, your knowledge and enthusiasm for physics is very inspiring. Thanks for always having time for discussions and questions, and guiding me in how to progress with the work. Andrea, thanks for always taking the time to answer my questions, hunting for factors of two, and somehow always knowing when I was in need of some encouraging words.

I also want to thank the rest of the research group for many interesting discussions. A special thanks to Samuel, who helped a lot with the project before it became a thesis, and also supported me whenever the cryostat needed (un)loading. I also direct my appreciation to the division of Solid State Physics and especially the community of master and PhD students that has been very warm and welcoming.

A thank you to all of my friends: for the daily walks, weekly lunches and five years of studying together that I have enjoyed immensely. And to my family, for never being further than a phone call away when I need some support, and for reminding me that there is life beyond studies and thesis work.

And lastly to my partner Hugo, thank you for giving the best hugs and always taking an interest and listening to my daily, way too detailed, accounts of how the measurements are going. Now you will finally get to hear the more coherent story of what I have been doing.

Contents

Chapter 1

Introduction

In the era of quantum science and technology, microwave signals have become of great importance. They provide the primary mechanism to interact with, control, and readout solid state systems ranging from superconducting qubits to spin qubits. Microwave photons are thus used both to transmit and store quantum information. To be able to read out the information from these systems, advanced detectors are needed, sensitive enough to detect the small energy of a microwave photon.

Such detectors must be able to distinguish between different photon statistics, which vary depending on the nature of the light source. Photons will exhibit either Poissonian, sub-Poissonian or super-Poissonian statistics. Photons of Poissonian statistics typically originates from a coherent light source, meaning that the electromagnetic field of the light can be modelled by a sinusoidal function. Sub-Poissonian statistics is exhibited by photons in number states and super-Poissonian statistics are seen in photons originating from a thermal distribution [1]. The super-Poissonian statistics of thermal photons means that they are more likely to arrive at a detector "bunched" together in time. A highly functional photon detector must be able to distinguish between photons originating from these different sources, and to test such a detector controllable photon sources are thus needed.

This thesis focuses on such a photon source, capable of emitting thermal photons, which is a process intrinsically linked to photonic heat conduction. In macroscopic systems, heat is primarily carried by phonons (lattice vibrations) and electrons. However, at temperatures typically below 150 mK, the electron-phonon relaxation process weakens significantly. Instead, photonic heat conduction, which is the transfer of heat via the emission and absorption of thermal microwave photons, becomes the dominating mechanism for thermal relaxation [2]. While single-mode heat conduction via photons has been experimentally realized in previous macroscopic and mesoscopic circuits [3, 4], it has so far yet to be measured directly. Creating a reliable, well-characterized thermal photon source provides an excellent test bed for studying this phenomenon.

The connection between the temperature of a material and the thermal photons it emits comes down to an effect in electronics that is called Johnson-Nyquist noise [5]. Essentially, any resistor at a finite temperature will exhibit spontaneous voltage fluctuations. These fluctuations will radiate thermal power into the connecting circuit. In the microwave regime, this radiation can be viewed as a stream of thermal photons. This means that a resistor can be used as a thermal photon source, where its temperature directly determines the amount of heat it radiates.

To create a thermal photon source and directly measure photonic heat conduction, this thesis uses a device with a metallic copper island acting as a variable thermal bath. This copper island also functions as a resistor, designed to be impedance-matched to the measurement setup. By ensuring this matched geometry between the device and the transmission lines, we aim to measure unity emission from the emitted signal out of the resistor. To study the emission from a thermal bath, we need to be able to probe the temperature of the copper island. However, measuring the temperature of such a microscopic structure in the millikelvin regime is not as simple as attaching a conventional thermometer. Instead, the device uses a Normal-Insulator-Superconductor (NIS) junction. The $I - V$ (current-voltage) characteristic of the NIS junction is highly sensitive to the electron temperature of the normal metal island, in our case the copper island, which allows us to study the emitted thermal microwave signal as a direct function of the resistor's temperature.

Turning to the opposite process compared to emission, this device can also be used to probe the radiation in the environment through absorption. In quantum systems, environmental noise and stray radiation lead to decoherence, which is directly detrimental to quantum measurements [6]. We demonstrate that the device can be used to show that introduction of additional filters to the measurement setup decreases the environmental radiation reaching the device. In this way, the device can also be considered as a bolometer, capable of detecting and quantifying ingoing radiation.

The outline of this thesis is as follows: First, an overview of the basic functionality of the device and the measurement setup is given in Chapter 2. This is followed by a description of the NIS junctions in Chapter 3. The chapter describes and derives both the theory that allows an NIS junction to work as a precise thermometer, as well as the measurements that characterizes the junctions and describes the thermometer function. Being able to perform accurate thermometry of the electronic temperature of the copper island provides the foundation for the emission and absorption presented in Chapter 4. This chapter presents measurement results showing near unity emission and absorption of the device together with a careful calibration of the microwave lines, as this directly influences the measurement precision. In Chapter 5, the theory behind the heat flow mechanisms in the device is derived, which is then compared to the actual measured heat flow. Lastly, a general discussion and outlook covering the preceding chapters is given in Chapter 6.

Chapter 2

Device and measurement setup

Before delving into the theory and measurements performed in the following chapters, we start by presenting the basic functionality of the device. We also give an overview of the measurement setup as well as an estimation of the resistance of the copper island.

At finite temperatures, any resistor exhibits spontaneous voltage fluctuations that exchange thermal power with a connected circuit. In the microwave regime, this energy transport can be viewed as the emission and absorption of discrete photons. Absorption of incoming photons heats the resistor, while the resistor's own temperature directly determines its rate of thermal photon emission. This is the underlying phenomenon that is used in this thesis to measure thermal emission.

2.1 Device

The measurements in this thesis has all been performed on the same device, shown in Fig. 2.1. Measurements were performed with the device connected to a sample holder with a PCB (printed circuit board), seen in Fig. 2.1a, and loaded into a dilution refrigerator, with a base temperature of 10 mK. The components of the measurement setup are therefore located at different temperatures, as shown in Fig. 2.1c. The device components of interest for this thesis are mainly the Normal-Insulator-Superconductor (NIS) junctions, the copper island and the microwave line, all shown in Fig. 2.1b.

2.1.1 Geometry

The device consists of a copper island which can be viewed as a resistor. The copper island connects to a superconducting aluminium line via a gold pad at the left side (Fig. 2.1b). The aluminium line functions as a microwave line where microwave photons can travel lossless to or from the island. At the right side, the island connects to an aluminium plane, via another gold pad (Fig. 2.1bc). This aluminium plane functions as a ground plane and is connected to the ground of the PCB (Fig. 2.1a), which in turn is connected to the ground of the outer shield of the connecting coaxial cable. The connection between the gold pads and aluminium forms clean, ohmic, NS (Normal-Superconductor) contacts.

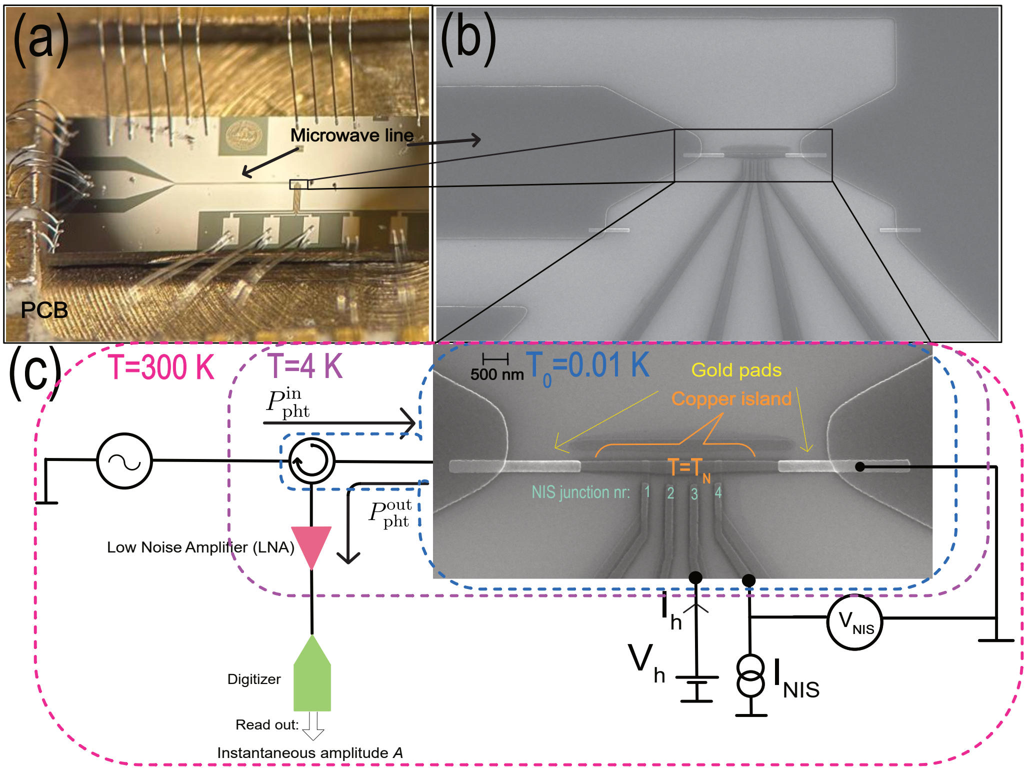

Figure 2.1: Images of device and measurement setup. (a) Device connected to the sample holder via bondwires. (b) Scanning Electron Micrograph (SEM) image of device. (c) SEM image of the device's copper island connected to four dc lines via NIS junctions, (numbered 1-4) and gold pads connecting the island to the microwave line (left) and ground (right). Junction 3 is used to heat the island by applying a voltage bias V_h, and junction 4 is used as a thermometer by applying a small constant current bias I_{NIS} and measuring the voltage V_{NIS}. The microwave line is connected to a microwave source, and can also be used to measure the outgoing amplified signal by use of a digitizer.

The dimensions of the normal metal structures are shown in Fig. 2.2, although the relative size between sides are not to scale.

Below the copper island in Fig. 2.1 are four superconducting aluminium leads, which conduct electrical signals without losses. These are connected to the island through NIS junctions, which means that instead of having clean NS junctions, there is a thin layer of oxide, in our case Al_2O_3, between the aluminium and the copper [2, 7]. The oxide creates a potential barrier and the junctions are thus tunnel junctions, where electrons have a certain probability of tunnelling between the superconductor and the normal metal. The resistance of an NIS junction is typically on the order of 50 kΩ [2].

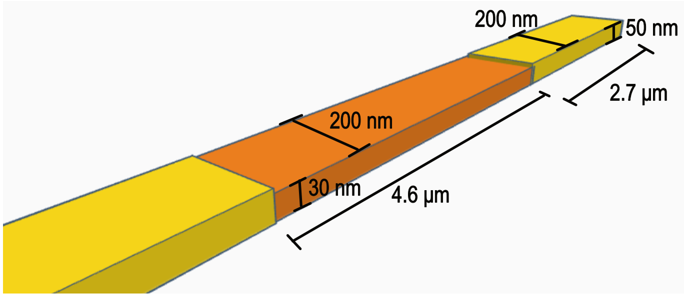

Figure 2.2: Schematic of the normal metal structure of the device, with marked dimensions. The copper island is illustrated in orange and the two gold pads in yellow. The two gold pads have the same dimensions. Note that the relative size between sides are not to scale.

2.1.2 Functionality

NIS junctions

The NIS junctions is used both to heat the island and probe the temperature of it in this thesis. The temperature can be probed by use of a current biased NIS junction. During the measurements performed in this thesis, junction 4 in Fig. 2.1c was typically used as a thermometer. The junction was current biased at a small constant current I_{NIS} and the voltage V_{NIS} over the junction was then measured. By using a small current bias, the self-heating effect of the thermometer will be negligible small [8] and is therefore ignored in this thesis. The voltage V_{NIS} that is measured over the junction will depend on the temperature of the normal metal, which is further explained in Chapter 3, and V_{NIS} can thus be used to infer the island temperature T_{NIS}. The interesting characteristics of NIS junctions arises from the differences in the density of state (DOS) and occupation of states between a normal metal and a superconductor. While the electron occupation in the normal metal will follow a Fermi distribution, the superconductor has no available electron states around the Fermi energy. The gap in the density of state is of size 2Δ, where Δ is the superconducting gap parameter. These characteristics will be further discussed in Chapter 3.

For heating, junction 3 in Fig. 2.1c has typically been used. The heating is typically performed by applying a voltage bias V_h to the junction, and measuring the current I_h running through the NIS junction. If a large voltage bias ($eV_h \gg \Delta$), is applied to the NIS junction it can be approximated to behave as a NIN junction, since the superconducting gap will be of little influence at this bias. The heating power can then be assumed to be symmetrically applied to the junction, i.e. the power $P = IV/2$ is applied to the island. At lower biases the heating power depends on the voltage bias in a more intricate manner, and is even theoretically predicted to cool the island if $eV \approx \Delta$ [8]. For simplicity, this thesis mainly uses heating in the high bias regime, where the applied heating power is easily determined.

Thermal emission and absorption

The microwave line is used to send in photons towards the island. Since the energy of microwave photons, with $f \lesssim 100$ GHz, is less than the superconducting bandgap, $hf < \Delta$, the photons can travel lossless through the superconducting aluminium [8]. Here h is Planck's constant and f is the frequency of the photon. A microwave photon that travels towards the copper island will either be absorbed by the island or reflected back through the line. The more well matched the resistance of the copper island is to the characteristic impedance of the measurement setup, the higher the probability is that the photon will be absorbed [4]. An absorbed photon will add the energy hf to the copper island in form of heat. Thus, microwave signals can be used to heat the copper island.

Just as a microwave photon can be absorbed by the copper island, one can also be emitted. The greater the temperature difference between the copper island and the surrounding environment, the larger the net amount of photons emitted into the microwave line. As a photon is emitted, the energy hf will leave the island and this emission is therefore a form of a heat flow [3, 4]. This heat flow is a type of stochastic voltage fluctuation that all resistive components exhibit, typically called Johnson-Nyquist noise [5]. The fluctuations are temperature dependent, and in the limit $hf \gg k_B T$, also frequency dependent. A photon emitted from these type of fluctuations will have a certain probability of being emitted respectively reflected when it reaches the NS interface, just as in the case of absorption. The emission probability depends on the matching between the resistance of the copper island and the measurement setup exactly as the absorption and the absorption- and emission probabilities are thus equal [5]. This thermal emission will be discussed and measured in Chapter 4.

Thermal isolation

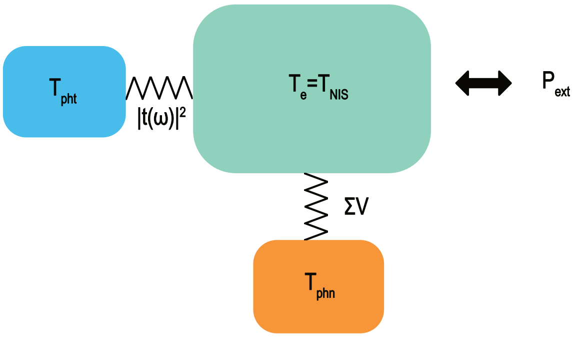

Figure 2.3: Simple thermal model of the device. The electron temperature on the normal metal island is $T_e = T_{\mathrm{NIS}}$, and is thermally coupled to the lattice phonons with the strength ΣV, where Σ is a coupling constant and V is the system volume. It is also coupled to the radiative environment, i.e. the photons. The photon temperature is T_{pht}, and the coupling constant $|t(\omega)|^2$, which describes the transmission probability at the angular frequency ω . The heat flow P_{ext} can also be supplied externally to the system.

The normal metal island will exchange heating through electron-phonon and electron-photon coupling, as shown in Fig. 2.3. Additionally, the external heating power P_{ext} will also affect the temperature of the island. The applied heating power P_{ext} is for instance an applied voltage bias V_h over an NIS junction or an ingoing microwave signal $P_{\text{pht}}^{\text{in}}$.

To be able to heat the copper island without heating its surroundings, it must be thermally isolated. With thermally isolated, we mean that the electrons on the island should be able to maintain a temperature T_e different from that of the phonons of the metal film or the substrate that the island is located on, a situation typically denoted as quasi-equilibrium. This become possible in small structures at low temperatures since the electron-phonon coupling then becomes very weak [8]. The heat flow through the electron phonon-coupling will depend on the volume V of the normal metal structures, shown in Fig. 2.2, and the electron-phonon coupling constant Σ which is material dependent [2]. The microwave line also connects the island to the radiative environment, and this electron-photon coupling gives rise to a second heat flow channel. Since superconductors are notoriously bad heat conductors at low temperatures, and unbiased NIS junctions only allows for very few electron tunneling events, the copper island is well isolated thermally from the surrounding systems [8].

2.2 Measurement setup

The device in Fig. 2.1c is connected to a PCB as shown in Fig. 2.1a, and loaded into a dilution refrigerator with a base temperature of around 10 mK. The signals that we are interested in measuring are the thermal photons emitted by the device, but our measurement instruments are located at room temperature. Some intermediate steps are therefore needed to be able to measure the emitted signal without it getting overpowered by thermal noise at room temperature.

An ingoing coherent microwave signal will be generated through an RF signal generator at room temperature. As it passes through the transmission lines on its way towards the device, the signal will be attenuated at several temperature stages. This means that the coherent signal which reaches the device will be much smaller than the one that is generated. This is done to avoid sending in thermal noise from 300 K. Since the noise is temperature dependent, the noise levels will be much larger at room temperature than at 4K or 10 mK, and this noise would overheat the device if it wasn't attenuated.

To measure an emitted microwave signal from the device we must first amplify the signal. The small emitted signal are otherwise easily overpowered by the thermal noise originating from the cabling as the signal progresses throughout the lines. Both the thermal emission originating from the device as well as from the cabling will typically be the same kind of stochastic Johnson-Nyquist noise, but as the cabling have a much higher temperature than the device, the noise from the cabling will be much stronger. Furthermore, due to the Fluctuation-Dissipation theorem, any noise that is dissipated will be replaced by the corresponding amount of noise from that resistive element [9]. It is therefore important to amplify the signal of interest as early on and at as low temperature as possible. In our setup this amplification is carried out by the Low Noise Amplifier (LNA) located at a temperature of 4K, and indicated in Fig. 2.1c as a pink triangle. Most of the cabling before this point is superconducting, to minimize the losses before the signal is amplified. At room temperature follows several stages of amplification, before the signal reaches the digitizer. The digitizer samples the signal which gives the final measurement value. To retain information about the original signal we must then backtrace the signal to the device again, which means that we need information about the components that are located along the signal path. This process is described in Chapter 4.

2.3 Estimating the absorption probability based on dc resistance

The probability that an ingoing photon is absorbed by the copper island is given by the standard microwave transmission coefficient [10]:

$$T = \frac{4RZ_0}{(R+Z_0)^2}, \tag{2.1}$$

where R is the resistance of the copper island and Z_0 is the characteristic impedance of the measurement setup. The probability for emitting a photon is simply the reverse process, which operates with this exact same probability [5]. This relationship shows that the emission and absorption of our device will approach unity if the resistance of the island is well-matched to the rest of the setup ($Z_0 = 50\ \Omega$).

To determine this probability experimentally, we measured the dc resistance of the copper island. This required a different setup compared to the one shown in Fig. 2.1. We used a 4-probe measurement, where the resistor was current biased and the voltage was measured over the island. The resistance of the island was found to be around 92 Ω. If the characteristic impedance for the measurement setup is assumed to be $Z_0 = 50\ \Omega$, Eq. (2.1) yields an absorption and emission coefficient of 91%. This estimate thus predicts that the emission and absorption of our device are close to unity.

Chapter 3

NIS junctions and thermometry

This chapter begins with a brief introduction to superconductivity and BCS theory, before deriving the temperature-dependent tunneling current through an NIS junction. Subsequently, measurements and characterization of the four junctions shown in Fig. 2.1 are presented. Finally, we focus on thermometry, detailing the working principle of an NIS thermometer and presenting $I - V$ characteristic measurements that demonstrate the thermal response of the junction when used as a thermometer.

An NIS junction consists of a normal metal (N) and a superconductor (S) separated by a thin insulating barrier (I). It acts as a tunnel junction, where an electron approaching the interface has a finite probability of tunnelling through the barrier. Due to the normal and superconducting density of states on either side of the insulating barrier the NIS junction exhibits a strong thermal sensitivity of the normal metal, while remaining insensitive to the temperature of the superconductor, rendering it a precise tool for temperature measurements.

3.1 Superconductivity

Introduction

A superconductor is a material that when cooled below a certain critical temperature T_c turns into a superconducting state. A normal conductor will have a resistance which decreases gradually as the temperature is lowered, but for a superconductor the resistance will drop to exactly zero below T_C. This characteristic gives rise to many interesting phenomena, such as for example persistent currents. Another characteristic of the superconductor is the Meissner effect, which is the complete expulsion of magnetic fields from a superconductor. This is often considered to be the fundamental property which describes superconductivity [11].

BCS theory

A microscopic theory explaining superconductivity was first presented in Ref. [12], and the theory was named after the authors as Bardeen-Cooper-Schieffer (BSC) theory. BSC theory is built on three principles:

- The effective forces between electrons in a solid can sometimes be attractive rather than repulsive
- Two electrons nearby the filled Fermi surface will bind together to form a stable pair, regardless of how weak the attractive force is. These paired electrons are called Cooper pairs
- All the Cooper pairs together form a many particle wave function which has the form of a coherent state wave function.

The BSC ground state wave function is a coherent state of Cooper pairs. The normalized BSC state can be written as

$$|\psi_{\text{BSC}}\rangle = \prod_k (u_k^* + v_k^* \hat{c}_{k\uparrow}^\dagger c_{-k\downarrow}^\dagger) |0\rangle , \tag{3.1}$$

where $|0\rangle$ denotes the vacuum state which in this case is the filled Fermi sea [11]. The electron creation operators $c_{k\uparrow}$, $c_{k\downarrow}$ together create a Cooper pair, which consists of two electrons with opposite spin and momentum. The normalizing constants u_k^* and v_k^* satisfy the normalization condition $|u_k|^2 + |v_k|^2 = 1$. The BSC ground states describes how for every k, there is a probability amplitude u_k^* that the state is empty and v_k^* that the state is occupied with a Cooper pair, i.e. every state is in an superposition of being empty and occupied. By minimizing the system's energy, these amplitudes are found to have a specific functional dependence on the electron energy ϵ_k

$$\begin{aligned} |u_k|^2 &= \frac{1}{2}\left(1 + \frac{\epsilon_k - \mu}{\sqrt{(\epsilon_k - \mu)^2 + |\Delta|^2}}\right) , \\ |v_k|^2 &= \frac{1}{2}\left(1 - \frac{\epsilon_k - \mu}{\sqrt{(\epsilon_k - \mu)^2 + |\Delta|^2}}\right) , \end{aligned} \tag{3.2}$$

such that states well below the Fermi energy are almost fully occupied, states well above are almost completely empty, and states near the Fermi level exist in a mixed superposition governed by the superconducting gap Δ [11]. Here μ denotes the chemical potential of the system, which equals the Fermi energy E_F at zero temperature.

The Hamiltonian for the effective interaction can be written as

$$\hat{H} = \sum_{k,\sigma} \epsilon_k c_{k\sigma}^\dagger c_{k\sigma} - |g_{\text{eff}}|^2 \sum_{k,k'} c_{k\uparrow}^\dagger c_{-k\downarrow}^\dagger c_{-k'\downarrow} c_{k'\uparrow}, \tag{3.3}$$

where the first part describes the energy of electron states, and the second describes the coupling of electrons into Cooper pairs that is the source of superconductivity. To simplify this Hamiltonian, we make use of a mean-field approximation called Wick's theorem which states that expectation values over four particle operators can be approximated by averages over two pairs [11]. Introducing $\Delta = |g_{\text{eff}}|^2 \sum_k \langle c_{-k\downarrow} c_{k\uparrow} \rangle$ then yields

$$\hat{H}_{\text{BCS}} = \sum_{k,\sigma} \epsilon_k c_{k\sigma}^\dagger c_{k\sigma} + \sum_k \left(\Delta c_{k\uparrow}^\dagger c_{-k\downarrow}^\dagger + \Delta^* c_{-k\downarrow} c_{k\uparrow} \right) . \tag{3.4}$$

This Hamiltonian can be diagonalized by use of a Bogoliubov transformation, where we introduce the new operators $\gamma^\dagger, \gamma$ as

$$\begin{aligned} \gamma_{k\uparrow} &= u_k^* c_{k\uparrow} - v_k^* c_{-k\downarrow}^\dagger \\ \gamma_{-k\downarrow}^\dagger &= v_k c_{k\uparrow} + u_k c_{-k\downarrow}^\dagger . \end{aligned} \tag{3.5}$$

The operators γ anticommute and have the eigenvalues $E_k = \sqrt{\epsilon_k^2 + |\Delta|^2}$. The diagonalized Hamiltonian then take the simple form

$$\hat{H}_{\text{BCS}} = \sum_{k,\sigma} E_k \gamma_{k\sigma}^\dagger \gamma_{k\sigma}. \tag{3.6}$$

The elementary excitations of a superconductor can thus be described by Bogoliubov quasiparticles, with the energy spectra $E_k = \sqrt{\epsilon_k + |\Delta|^2}$. Adding or removing one of these quasiparticles to the superconductor will cost $\pm E_k$ compared to $\pm \epsilon_k$ in the normal state. The minimum energy to make an excitation is 2Δ, which can thus be seen as the energy gap of the superconductor.

Density of states

When a material transitions from normal into superconducting, the total number of states is preserved. A state with energy ϵ before the transition will have the energy E after the transition, which means that the states in an interval $d\epsilon$ before the transition all must end up in the interval dE after the transition. The normal state DOS and superconducting DOS must hence fulfil

$$N_N(\epsilon) d\epsilon = N_S(E) dE, \tag{3.7}$$

where $N_N(\epsilon)$ is the normal state density of state (DOS) and $N_S(E)$ is the superconducting density of state. For the superconductor the region of interest for the density of state is a small range close to the Fermi level, over which we can assume the normal DOS to be more or less constant, $N_N(\epsilon) \approx N_N$. With this, we obtain

$$N_S(E) = N_N \frac{d\epsilon}{dE} = N_N \frac{E}{\sqrt{E^2 - \Delta^2}}. \tag{3.8}$$

This expression is valid for $E > \Delta$. For $E < \Delta$ we instead have $N_S(E) = 0$ as there are no quasiparticle states within this energy range. When drawn, $N_S(E)$ is typically mirrored around the Fermi level, which can be interpreted as taking both electrons and holes into consideration. The superconducting DOS is shown in Fig. 3.2.

3.2 Tunnelling current through an NIS junction

An NIS junction will have the normal metal DOS on one side of the tunnelling barrier, and a superconducting DOS on the other side. This creates some rather interesting characteristics of the tunnelling current, since the superconducting gap will prohibit the electrons at the Fermi energy on the N side to tunnel into the S side when the junction is unbiased.

In this section, we will derive the tunnelling current through an NIS junction, starting from the Hamiltonian of the system. The derivation is based on Ref. [13].

To derive the tunnelling current through the NIS junction we start by defining the Hamiltonian of the system:

$$\hat{H} = \hat{H}_S + \hat{H}_N + \hat{H}_T, \tag{3.9}$$

where $\hat{H}_S$ is the superconducting hamiltonian of Eq. (3.6). $\hat{H}_N$ is the Hamiltonian for the normal metal

$$\hat{H}_N = \sum_{k\sigma} \epsilon_k a^\dagger_{k\sigma} a_{k\sigma}, \tag{3.10}$$

where $a^\dagger_{k\sigma}$ and $a_{k\sigma}$ are fermionic operators describing the creation and annihilation of an electron with wave vector k and spin σ. $\hat{H}_N$ can be obtained from $\hat{H}_S$ by taking the limit $\Delta = 0$. The tunnelling Hamiltonian $\hat{H}_T$ describes the electron tunnelling between the superconductor and normal metal and reads

$$\hat{H}_T = \sum_{kq\sigma} \left(t_{kq} c^\dagger_{q\sigma} a_{k\sigma} + t^*_{kq} a^\dagger_{k\sigma} c_{q\sigma} \right), \tag{3.11}$$

where t_{kq} describes the strength of the tunnelling coupling between the N and S side, i.e. how transparent the barrier is. The first term of $\hat{H}_T$ describes an electron tunnelling from the normal metal to the superconductor, while the second term instead corresponds to an electron tunnelling the opposite way. The spin σ is preserved through the tunnelling event as we assume the coupling to be spin conserving.

Next, we need to define the current operator $\hat{I}$ which can be done by viewing time evolution in the Heisenberg picture, and using that current is defined as charge per time. The number operator for electrons in the normal metal is $\hat{N}_N = \sum_{k\sigma} a^\dagger_{k\sigma} a_{k\sigma}$ and using this the current operator can be obtained as

$$\hat{I} = e\frac{d}{dt}\hat{N}_N = \frac{ie}{\hbar}[\hat{H}, \hat{N}_N] = \frac{ie}{\hbar}[\hat{H}_N, \hat{N}_N] = \frac{ie}{\hbar}\sum_{kq\sigma} \left(t_{kq} c^\dagger_{q\sigma} a_{k\sigma} + t^*_{kq} a^\dagger_{k\sigma} c_{q\sigma} \right), \tag{3.12}$$

where we use that both $\hat{H}_S$ and $\hat{H}_N$ commutes with $\hat{N}_N$. The last equality follows from calculating the commutator by using the anticommutator rules for fermionic operators, together with $a^\dagger a^\dagger = aa = 0$.

To calculate the dc current $I = \left\langle \hat{I} \right\rangle$ we use the Kubo formula which is an expression for the linear response of an observable quantity when disturbed by a small perturbation [14]. This yields

$$I = \left\langle \hat{I} \right\rangle = \frac{i}{\hbar}\int_{-t_0}^{t} dt' \left\langle [\hat{H}_T(t'), \hat{I}(t)] \right\rangle_0 . \tag{3.13}$$

Using the expressions for $\hat{H}_T$ and $\hat{I}$, described in Eq. (3.11) and Eq. (3.12), the commutator yields

$$\begin{aligned} [\hat{H}_T(t'), \hat{I}(t)] = \frac{ie}{\hbar}\sum_{kq\sigma} |t_{kq}|^2 (&a^\dagger_{k\sigma}(t) c_{q\sigma}(t) c^\dagger_{q\sigma}(t') a_{k\sigma}(t') + a^\dagger_{k\sigma}(t') c_{q\sigma}(t') c^\dagger_{q\sigma}(t) a_{k\sigma}(t) \\ &- c^\dagger_{q\sigma}(t) a_{k\sigma}(t) a^\dagger_{k\sigma}(t') c_{q\sigma}(t') - c^\dagger_{q\sigma}(t') a_{k\sigma}(t') a^\dagger_{k\sigma}(t) c_{q\sigma}(t)), \end{aligned} \tag{3.14}$$

where the first two terms correspond to an electron tunnelling from the normal metal into the superconductor ($N \rightarrow S$) and the two last terms instead correspond to an electron tunnelling from $S \rightarrow N$.

Let's start by calculating the current from $N \rightarrow S$. To calculate the expectation value of this operator we then need to perform the Bogoliubov transformation on the c operators as in Eq. (3.5). The expectation value of this expression can be evaluated in the Heisenberg picture, which factors out the time dependence of the annihilation operators as $a_k(t) = e^{-i\epsilon_k t/\hbar} a_k$ and $\gamma_{q\sigma}(t) = e^{-iE_q t/\hbar}\gamma_{q\sigma}$ and the Hermitian conjugate of these for the creation operators. Here $\epsilon_k = \frac{\hbar^2 k^2}{2m}$ is the energy of an electron in the normal metal with wave vector k, while $E_q = \sqrt{\epsilon_{\pm q}^2 + \Delta^2}$, $\epsilon_q = \frac{\hbar^2 q^2}{2m}$ is the energy of an electron with wave vector q in the superconductor, where Δ denotes the gap energy. This yields the current as

$$\begin{aligned} I_{N\rightarrow S} &= \frac{e}{\hbar^2}\int_{-t_0}^{t} dt' \sum_{kq\sigma} |t_{kq}|^2 \, \{ \left\langle a_{k\sigma}^\dagger(t) c_{q\sigma}(t) c_{q\sigma}^\dagger(t') a_{k\sigma}(t') \right\rangle_0 \\ &\qquad + \left\langle a_{k\sigma}^\dagger(t') c_{q\sigma}(t') c_{q\sigma}^\dagger(t) a_{k\sigma}(t) \right\rangle_0 \Big\} \\ &= \frac{e}{\hbar^2}\int_{-t_0}^{t} dt' \sum_{kq\sigma} |t_{kq}|^2 \, \{ |v_{q\sigma}|^2 \left\langle a_{k\sigma}^\dagger \gamma_{-(q\sigma)}^\dagger \gamma_{-(q\sigma)} a_{k\sigma} \right\rangle_0 e^{i(\epsilon_k + E_q)(t-t')} \\ &\qquad + |u_{q\sigma}|^2 \left\langle a_{k\sigma}^\dagger \gamma_{q\sigma} \gamma_{q\sigma}^\dagger a_{k\sigma} \right\rangle_0 e^{i(\epsilon_k - E_q)(t-t')} \\ &\qquad + |v_{q\sigma}|^2 \left\langle a_{k\sigma}^\dagger \gamma_{-(q\sigma)}^\dagger \gamma_{-(q\sigma)} a_{k\sigma} \right\rangle_0 e^{-i(\epsilon_k + E_q)(t-t')} \\ &\qquad + |u_{q\sigma}|^2 \left\langle a_{k\sigma}^\dagger \gamma_{q\sigma} \gamma_{q\sigma}^\dagger a_{k\sigma} \right\rangle_0 e^{-i(\epsilon_k - E_q)(t-t')} \Big\} . \end{aligned} \tag{3.15}$$

We can now perform the time integration to turn the exponentials into delta functions, by letting $t_0 \rightarrow \infty$ and performing the variable change $\tau = t - t'$

$$\begin{aligned} &\int_{-t_0}^{t} dt' (e^{i(\epsilon_k \pm E_q)(t-t')/\hbar} + e^{-i(\epsilon_k \pm E_q)(t-t')/\hbar}) \\ &= \int_{-\infty}^{\infty} d\tau e^{i(\epsilon_k \pm E_q)\tau/\hbar} = 2\pi\hbar\delta(\epsilon_k \pm E_q). \end{aligned} \tag{3.16}$$

Furthermore, the sums in equation Eq. (3.15) can be turned into integrals over ϵ_k and E_q,

$$\sum_{k\sigma} \rightarrow N_N \int d\epsilon_k, \tag{3.17}$$

where N_N is the normal state density of state, which we can assume to be constant over the relative energy range, and accounts for both spins. For the sum over q, we instead get

$$\sum_q = N_N \int d\epsilon_q = N_N \int dE_q \frac{E_q}{\sqrt{E_q^2 - \Delta^2}} = N_N \int dE_q N_S(E_q), \tag{3.18}$$

where in the last step the superconducting density of state $N_S(E)$ has been identified. Finally, Eq. (3.15) becomes

$$\begin{aligned} I_{N\rightarrow S} =& \frac{2\pi e}{\hbar} N_N^2 |t_{kq}|^2 \int dE N_S(E) \int d\epsilon \left\{ |v|^2 \left\langle a_{k\sigma}^\dagger a_{k\sigma} \gamma_{-(q\sigma)}^\dagger \gamma_{-(q\sigma)} \right\rangle_0 \delta(\epsilon + E) \right. \\ & \left. + |u|^2 \left\langle a_{k\sigma}^\dagger a_{k\sigma} \gamma_{q\sigma} \gamma_{q\sigma}^\dagger \right\rangle_0 \delta(\epsilon - E) \right\} , \end{aligned} \tag{3.19}$$

where we denote $E = E_q$ and $\epsilon = \epsilon_k$ for simplicity. Carrying out the integration over ϵ removes the delta functions. To evaluate the remaining expectation values, we use the fact that the normal electron operators a_k and the superconducting quasiparticle operators γ_q describes two independent systems in thermal equilibrium at temperatures T_N and T_S, respectively. Using fermionic anticommutation rules, their thermal expectation values yield the respective Fermi-Dirac distributions $\left\langle a_k^\dagger a_k \right\rangle = f_N(\epsilon)$ and $\left\langle \gamma_k^\dagger \gamma_k \right\rangle = f_S(E)$. Substituting these changes into Eq. (3.19) simplifies the expression to

$$\begin{aligned} I_{N\to S} = \frac{2\pi e}{\hbar} N_N^2 |t_{kq}|^2 \bigg(\int dE n_S(E) |v|^2 f_N(-E) f_S(E) + \\ + \int dE N_S(E) |u|^2 f_N(E)(1 - f_S(E)) \bigg) = \dots \\ = \frac{1}{eR_T} \int_{-\infty}^{\infty} dE N_S(E) f_N(E)(1 - f_S(E)), \end{aligned} \tag{3.20}$$

where the variable change $E' = -E$ is performed for the v term, and the relation $1 = |v|^2 + |u|^2$ is used. The subindices S and N for the Fermi functions denotes the superconductor and normal metal. Furthermore, the constants are collected into the term R_T, which experimentally is the tunnelling resistance of the junction.

In this derivation, the junction has been assumed to be unbiased. If a voltage bias V_b is applied to an NIS junction, this will shift the potential of the normal side of the junction with $-eV_b$ relative to the superconducting side [13], thus yielding the current

$$I_{N\to S} = \frac{1}{eR_T} \int_{-\infty}^{\infty} dE n_S(E) f_N(E - eV_b)(1 - f_S(E)). \tag{3.21}$$

The derivations for $I_{S\to N}$ can be performed in a similar manner, with the resulting current

$$I_{S\to N} = \frac{1}{eR_T} \int_{-\infty}^{\infty} dE n_S(E)(1 - f_N(E - eV_b)) f_S(E). \tag{3.22}$$

The total current into the superconductor can then be calculated as $I = I_{N\to S} - I_{S\to N}$ which gives the final expression for the current as

$$\begin{aligned} I(V) =& \frac{1}{eR_T} \int_{-\infty}^{\infty} dE n_S(E) \left(f_N(E - eV) - f_S(E) \right) \\ =& \frac{1}{2eR_T} \int_{-\infty}^{\infty} dE n_S(E)(f_N(E - eV) - f_N(E + eV)). \end{aligned} \tag{3.23}$$

The second expression shows that the current through the NIS junction is insensitive to the temperature of the superconductor, but dependent on the normal metal temperature. Therefore, the NIS junction can be used to probe the temperature of the normal metal side of the junction. Fig. 3.1 presents measured $I - V$ curves for the four junctions on the device, shown together with Eq. (3.23) as solid lines.

3.3 Experimental characterization of NIS junctions

The device has four NIS junctions, which will all have slightly different properties. By applying a voltage V and measuring the current I through the junction, the junctions

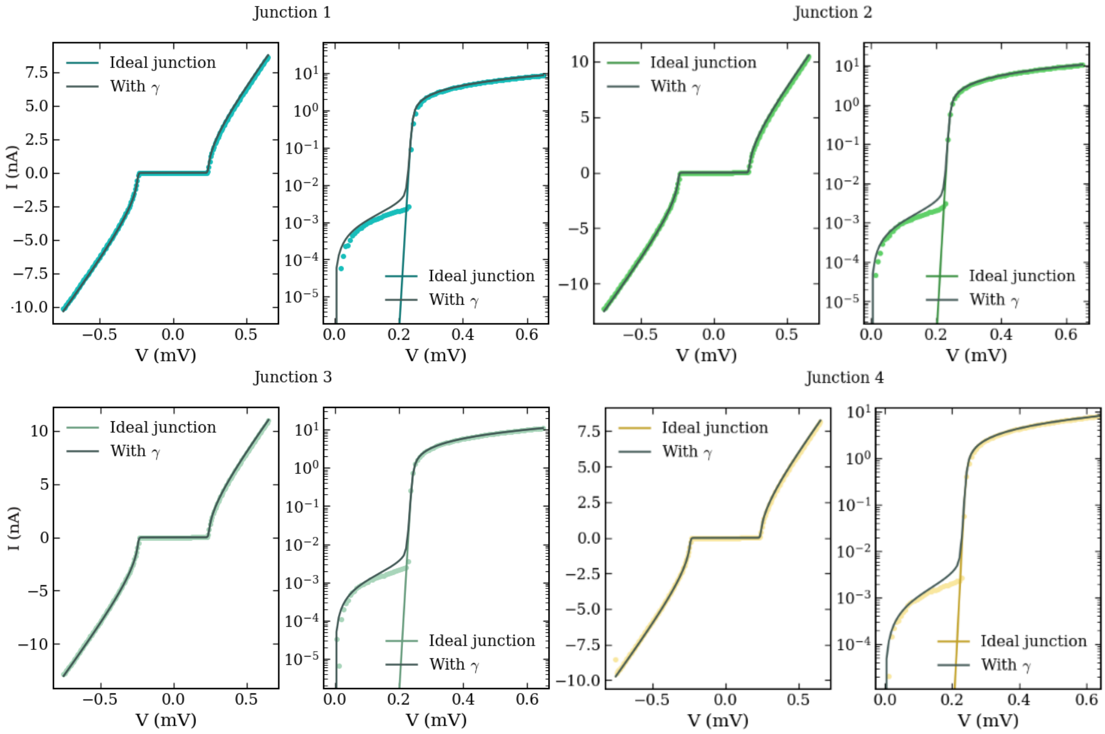

Figure 3.1: IV characteristics of the four NIS junctions at base temperature, measured by sweeping the voltage and measuring the current. The lines show theoretical fits using Eq. (3.23) and the parameters in Table 3.1, where for $1.1 \cdot R_T$ has been used for the resistance to get a good fit, and the base temperature is assumed to be 35 mK. Fits are shown both for an ideal junction and including the Dynes parameter γ. The current is plotted in log scale in the right panels, so that the characteristics at low currents become visible.

can be characterized and the normal state resistance R_T, Dynes parameter γ and superconducting gap parameter Δ determined. The Dynes parameter γ describes additional leakage at low bias voltage by adding a lifetime broadening $E \rightarrow E + i\gamma$ to the DOS of Eq. (3.8) [15].

Fig. 3.1 represents the measured $I - V$ curves of the four NIS junctions together with fits of Eq. (3.23). The normal state tunnelling resistance R_T is best found by applying a large bias, which renders the effect of the superconducting gap negligible. Here the junction thus behaves as in the normal state, and the resistance approaches the tunnelling resistance, $R_T \approx V/I$. This is the inverse slope at high bias in the left panels of Fig. 3.1. At a bias voltage $|V| < \Delta/e$ the tunneling current will be suppressed, as there are no electron states within the superconducting gap Δ, but once $|V| > \Delta$ a current flows. This explains why $I \approx 0$ around $V = 0$. The superconducting gap parameter is determined to be $\Delta = 240$ μeV for all four junctions, through fitting of Eq. (3.23) to the experimental data.

In an ideal BSC superconductor, there are no quasiparticle states within the superconducting gap, and we can see from Eq. (3.23) that this should result in an exponentially suppressed current for $-\Delta < V < \Delta$. In experiments however, a small current, linear in voltage, often persists even at small biases [16]. Such a current is seen in the right panels in Fig. 3.1, where the current saturates around $1 \times 10^{-3} - 1 \times 10^{-4}$ nA at a bias $V < \Delta$, rather than following the fit for the ideal junction. This subgap current is typically quantified through the dimensionless Dynes parameter γ which can be found from the ratio of R_T and the measured zero bias resistance R_{subgap} of the junction, i.e. $\gamma = R_T/R_{\text{subgap}}$ [17].

The subgap current is often explained through the introduction of Dynes DOS

$$N_s^D(E) = \text{Re}\left\{ \left(\frac{E/\Delta + i\gamma}{\sqrt{(E/\Delta + i\gamma)^2 - 1}} \right) \right\}, \tag{3.24}$$

which is a lifetime-broadened version of the BCS DOS. A nonzero γ effectively introduces states within the superconducting gap. The Dynes DOS may for instance arise as an result of photon assisted tunnelling [16].

Junction	1	2	3	4
Normal state resistance, R_T	69.0 kΩ	57.0 kΩ	54.7 kΩ	73.0 kΩ
Dynes parameter, γ	$6.9 \cdot 10^{-4}$	$5.7 \cdot 10^{-4}$	$5.5 \cdot 10^{-4}$	$7.1 \cdot 10^{-4}$
Superconducting gap, Δ	240 μV	240 μV	240 μV	240 μV

Table 3.1: Fit parameters of the 4 junctions. γ is extracted as the ratio of the slope in the high and low bias regime respectively, while Δ and R_T is found from the fitting of Eq. (3.23). The theoretical fits resulting from these parameters are shown in Fig. 3.1

.

The parameters used for the theoretical fits in Fig. 3.1 are shown in Table 3.1. There is some flexibility to the fit, and the superconducting gap Δ could for example be lowered a few μV without too much of a difference in the fit, but already at $\Delta = 235$ μeV the correspondence between theoretical and experimental data got worse. The normal metal temperature has been fitted as $T_N = 35$ mK based on the exponential suppression of current in the curves. This is in good correspondence with measurements performed later, where the base temperature of the normal metal island was measured to saturate at $T_0 = 35$ mK when varying the cryostat temperature T_0 in later experiments.

In Fig. 3.1, we evaluate how well Eq. (3.23) models the measured current through the NIS junctions. In the linear plots (left panels), the over all correspondence shows good agreement. To examine the behaviour at small currents, the data is also plotted on a logarithmic scale (right panels). Here, the fit remains robust, with only slight deviations near the gap edge where the idealized model and the model incorporating the Dynes parameter γ diverge. Most importantly, the extracted temperature T_N and superconducting gap Δ appear accurate. Adjusting the gap parameter shifts the steep exponential onset horizontally, while varying the temperature T_N in Eq. (3.23) alters its slope. Because the measured data closely follows this theoretical exponential slope, the chosen parameters describe the junctions well.

3.4 Thermometry

3.4.1 NIS junction as a thermometer

As was concluded from Eq. (3.23), the IV characteristics of an NIS junction is insensitive to the temperature of the superconducting side of the junction, but sensitive to the temperature of the normal metal. Hence, it can be used as a thermometer of the copper island, as is done in this thesis. A more intuitive understanding of the NIS thermometer can be obtained from studying the energy diagrams of the normal metal and superconducting side of the junction. Such energy diagrams, together with their corresponding voltage-current point in an IV sweep are shown in Fig. 3.2. If the normal side has a low temperature, the Fermi distribution will be close to rectangular and then a current can only run through the junction once the voltage bias is close to the superconducting gap, $eV = \Delta$ (Fig. 3.2ab). However, as the temperature increases, the Fermi distribution becomes more spread out, which means that there is a higher probability of finding electrons with energy higher than the Fermi energy (and a symmetrical argument for the holes). Hence, the same current as for the low-temperature case can now be obtained at a lower voltage bias (Fig. 3.2cd). By keeping the current fixed at the level indicated by the black dots in Fig. 3.2b-d, and measuring the voltage over the junction, a precise reading of the normal metal temperature can thus be obtained.

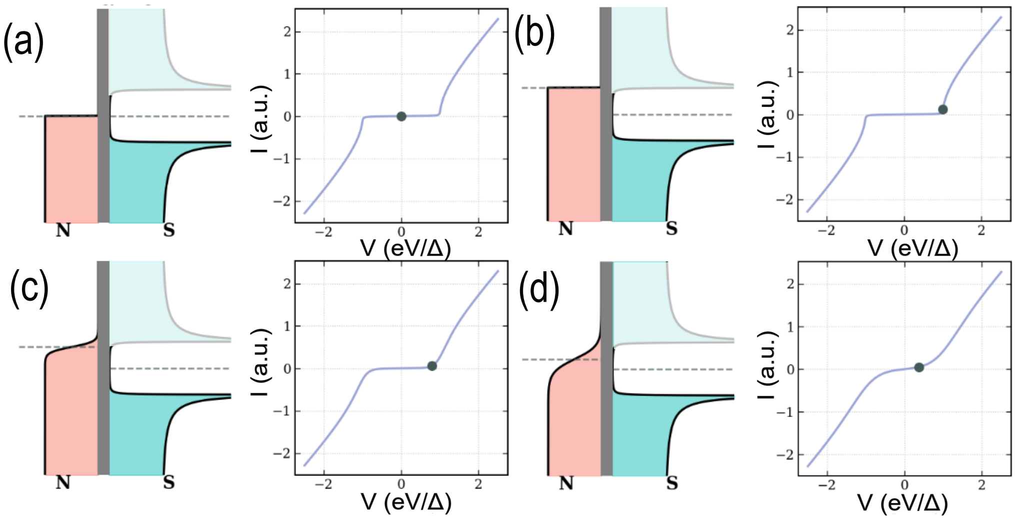

Figure 3.2: Working principle for the NIS thermometer. Energy diagram shows the Fermi distribution of the normal metal (pink) and the superconducting density of state (turquoise). The lighter shade of the superconductor indicates that the states are unoccupied. The corresponding current/voltage point is showed in the IV characteristic. (a) At low temperature and no bias, no electrons can tunnel through the junction. (b) At low temperature, a high bias is needed to have a tunnelling current. (c) and (d) As the temperature is increased, the Fermi distribution becomes more smeared and less bias is needed for the electrons to tunnel through the junction.

3.4.2 Temperature sensitivity

Thermal response

To study the response of the NIS junction when the temperature T_N of the copper island is increased, we can vary the bath temperature T_0 of the dilution refrigerator and measure the $I-V$ curves. The result is presented in Fig. 3.3. Varying T_0 changes the temperature of the whole device and its surroundings, including the temperature of the normal metal. However, the electronic temperature of island typically saturates at low bath temperatures, due to leakage heat flows resulting, for example, from coupling to the environment. This means that we likely have $T_N > T_0$ for example at the base temperature $T_0 = 10$ mK. Hence, we cannot take for granted that $T_N = T_0$ at low temperatures. In Fig. 3.3 the thermal response of the current biased NIS junction is shown, when the bath temperature T_0 was varied. The experimental data is plotted together with a theoretical fit using Eq. (3.23) and the fitting parameters in Table 3.1. We can see in the figure that the fit is reasonably good at $T_0 = 50$ mK, which indicates that the saturation temperature of the island is lower than 50 mK.

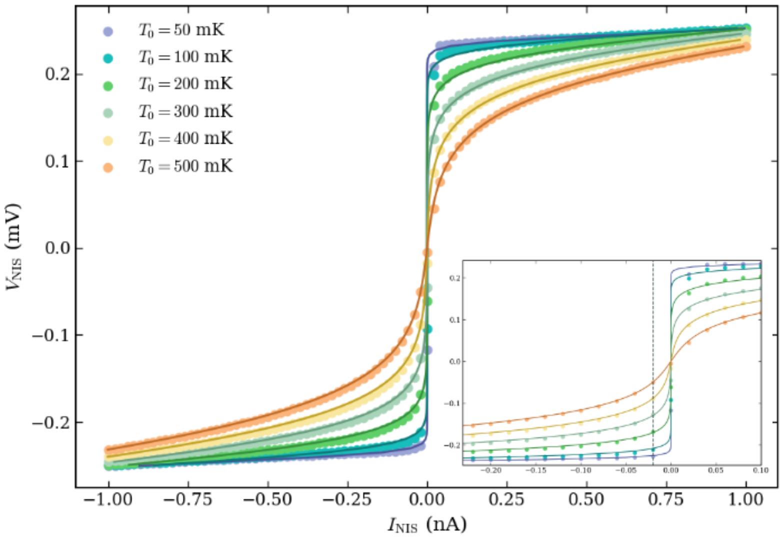

Figure 3.3: Change in $I-V$ characteristics for junction 4 as the temperature T_0 is varied. The dots show experimental data, measured by sweeping the current bias I_{NIS} and measuring the voltage V_{NIS}. The lines show the theoretical fit, using Eq. (3.23) and the parameters of junction 4 in Table 3.1, together with the temperature T_0. Inset shows how the voltage V_{NIS} changes with temperature at the thermometer biasing point $I_{NIS} = -20$ pA, marked with a dashed line.

Operation point

By current-biasing one of the junctions, the measured voltage drop across it becomes highly sensitive to the electron temperature of the normal metal, allowing the junction to operate as a precise thermometer. For the measurements in this thesis, junction 4 (Fig. 2.1) is utilized as the thermometer, biased at a constant current of $I_{NIS} = -20$ pA. This specific current is chosen because it lies on the steepest part of the $I-V$ curve (as seen in the logarithmic plots of Fig. 3.1), which maximizes the temperature sensitivity. Furthermore, the current bias should be small to minimize the heating it contributes with to the island. However, the chosen current I_{NIS} is still large enough to keep the measurement safely outside the low-bias regime, where the current is dominated by temperature-independent subgap leakage. The thermal response of V_{NIS} for $I_{\mathrm{NIS}} = -20$ pA is shown in the inset of Fig. 3.3.

Calibration

In order to use the NIS junction as a thermometer, the correspondence between measured voltage V_{NIS} and the island temperature T_{N} needs to be known. This can of course be modelled through Eq. (3.23) but to get a more reliable conversion, it is better to calibrate the thermometer by varying the bath temperature T_0.

The calibration should also yield information about the saturation temperature of the island. To minimize the environmental noise that reaches the device, circulators and filters are used. For the first setup that the thermometer calibration was carried out on, the saturation temperature was found to be around 65 mK, as seen in the inset of Fig. 3.4. In an attempt to lower the saturation temperature, two additional filters were installed on the outgoing microwave line. When the thermometer was calibrated again, the saturation temperature was found to be lower, around 35 mK (Fig. 3.4). The impact that this change of setup had on the saturation temperature shows the necessity of proper filtering to reach as low base temperature T_0 as possible. Overall, the measured data follows the theoretical fit from Eq. (3.23) fairly well, apart from below the saturation temperature.

In figure Fig. 3.4 all the temperature - voltage points measured during calibration are shown. The measured data seems to follow a linear relation between $35-500$ mK, and in the following when T_{NIS} is mentioned, it will be extracted from the linear relation between T_0 and V_{NIS} that is interpolated from this data. Thus the temperature range $35-500$ mK, where the linear interpolation works well, will be used for measurements in this thesis.

3.5 Probing the temperature T_{N} of the heated island with an NIS junction

The following chapters of this thesis relies on that we are able to heat the normal metal island locally, i.e. without changing the bath temperature T_0, and then measure the temperature T_{N} using the current biased NIS thermometer. To distinguish the temperature measured by the NIS junction from the one that can be inferred from the photon emission in Chapter 4, we will denote it as T_{NIS}.

NIS junctions has been used to heat a normal metal island in several previous experiments [3, 4, 18]. More recently, also an ingoing microwave signal has been used for the same purpose. Such measurements have been performed to measure the resonance frequency of a superconducting circuit [19], and also to study coherence effects in heat transport [20], by measuring the temperature of the thermally isolated island as a function of the frequency

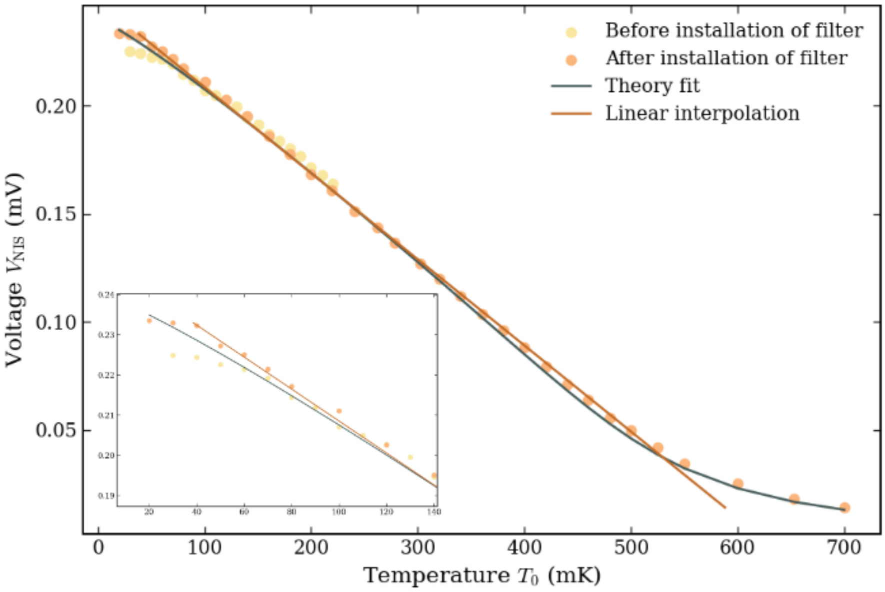

Figure 3.4: Thermometer calibration. Measured voltage V_{NIS} when junction 4 is current biased with $I_{\mathrm{NIS}} = -20$ pA for different cryostat temperatures T_0. The measurement was performed both before and after two additional filters were installed inside the cryostat. The grey line shows the theoretical fit using Eq. (3.23) and the parameters of junction 4 in Table 3.1. The linear interpolation, used to convert V_{NIS} to T_{NIS} is plotted as an orange line. The inset shows the low temperature regime and the experimental temperature saturation.

of the ingoing microwave signal. This thesis will rather focus on the thermal properties, such as emission and heat flow, of the device as a function of the island temperature T_{NIS} and applied heating power.

In Fig. 3.5 the thermal response to an ingoing microwave signal of different powers $P_{\mathrm{in}}^{\mathrm{pht}}$ is shown. The calibration for the ingoing power will be presented in Section 4.3. The current I_{NIS} is swept to generate a full $I-V$ curve, and the voltage V_{NIS} over the junction is measured. The $I-V$ curves show good correspondence with theoretical fits at the same temperatures, confirming that the measured voltage V_{NIS} that is converted to a temperature T_{NIS} is indeed the result of a genuine thermal response. Furthermore, this measurement confirms that the island is thermally isolated, as we are indeed able to heat it with an ingoing microwave signal, which will allow us to study emission and heat flows in the two following chapters.

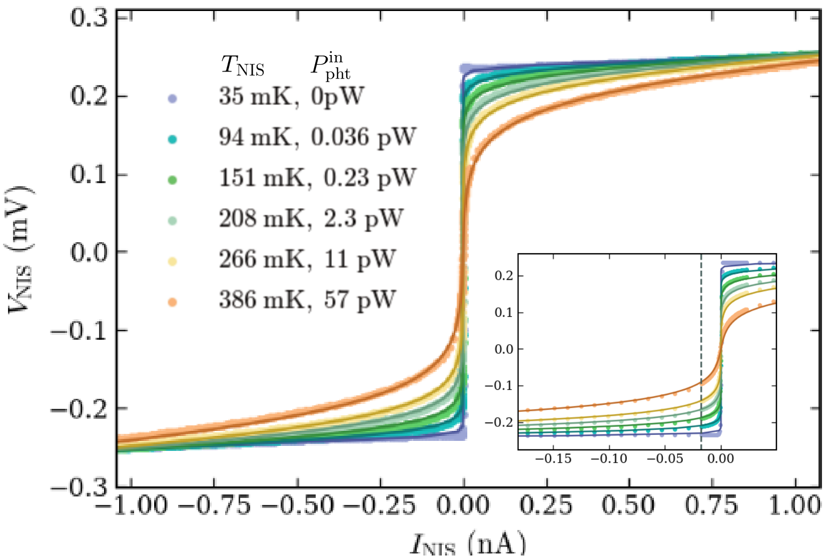

Figure 3.5: Thermal response of the thermometer junction (junction 4). The dots show experimental data, and is measured by sweeping the current bias I_{NIS} and measuring the voltage V_{NIS}. The lines show the theoretical fit, using Eq. (3.23) and the parameters of junction 4 in Table 3.1, together with the temperature T_{NIS} measured at $I_{\text{NIS}} = -20$ pA. The copper island has been heated through absorption of an microwave signal with power $P^{\text{in}}_{\text{pht}}$. Inset shows how the voltage V_{NIS} changes with temperature at the thermometer biasing point $I_{\text{NIS}} = -20$ pA, marked with a dashed line.

Chapter 4

Thermal noise and unity emission

In the previous chapter, a current-biased NIS junction was proven to be a precise thermometer for the copper island. In this chapter, we will study the thermal noise emitted from a resistor at 5 GHz and 7.5 GHz as a function of the temperature measured with this NIS junction. We first show that the absorption efficiency at these frequencies is close to 100%, which suggests that it should be possible to measure a close-to-unity thermal photoemission from the resistor. We then proceed to show measurements demonstrating the successful implementation of this thermal photoemitter.

This chapter covers the derivation of Johnson-Nyquist noise, measurements of the absorption efficiency, and the details of the noise calibration setup. It concludes by demonstrating the main result of near-unity thermal emission.

4.1 Johnson-Nyquist noise

Johnson-Nyquist noise is random thermal motion of charge carriers that arises in all resistive components. It was first derived in the classical regime in [5], where the generalization to the quantum limit was then obtained by considering that the energy per degree of freedom follows the Bose-Einstein distribution. In the derivation below we take inspiration from [4] and follow the reverse approach, starting from the quantum regime and concluding with a simplified expression that holds in the classical regime ($k_B T \gg hf$). Before this, we however first give a quick review on how the field in a transmission line can be quantized.

Derivation

The setup that we consider is shown in Fig. 4.1a and consists of a resistor with resistance R that describes the copper island. The resistor is coupled to a transmission line, which corresponds to the copper island coupled to the outgoing microwave line. The outgoing transmission line continues indefinitely long, and can therefore be considered to be semi-infinite. In a similar manner, the resistor can also be treated as a semi-infinite transmission line, extending from $x = 0$ to $x = \infty$ with characteristic impedance $Z = R$ [21]. This

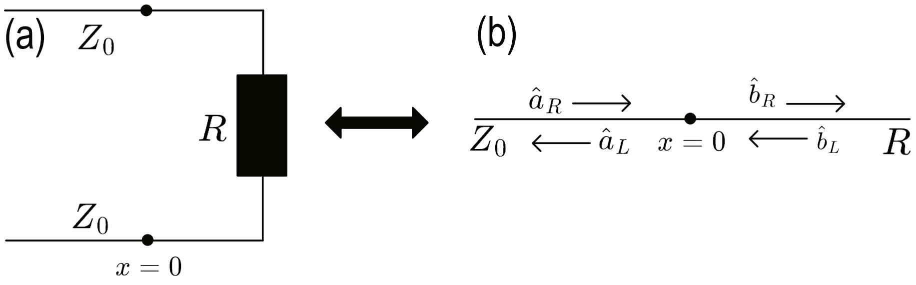

Figure 4.1: The measurement setup considered in the derivation of Johnson-Nyquist noise. (a) Simplified circuit diagram of the resistor connecting to the transmission line. (b) The resistor modelled as a semi-infinite transmission line, connecting to the real transmission line at $x = 0$. The definition of the left- and right moving wave amplitude operators is also shown.

model is shown in Fig. 4.1b. At the boundary point $x = 0$ the semi-infinite transmission line will appear as a resistor where an electrical wave travelling to the right towards ∞ will act as energy dissipated in the resistor. Similarly, an electrical wave moving towards the left can be seen as power emitted from the resistor. At $x = 0$ the resistor connects to a transmission line with characteristic impedance Z_0, which represents the outgoing microwave line in our measurement setup.

We can now consider the quantization of the field in the transmission line. Let's start by viewing the waves classically, and define the wave amplitudes of the left and right moving waves as

$$\begin{aligned} A_{\rightarrow}(x,t) &= \frac{1}{2}\left[\frac{1}{\sqrt{Z_c}}V(x,t) + \sqrt{Z_c}I(x,t)\right] \\ A_{\leftarrow}(x,t) &= \frac{1}{2}\left[\frac{1}{\sqrt{Z_c}}V(x,t) - \sqrt{Z_c}I(x,t)\right], \end{aligned} \tag{4.1}$$

where we have defined the characteristic impedance as $Z_c = \sqrt{L_l/C_l}$ and L_l and C_l are the characteristic inductance and capacitance per unit length. These fields can be turned into operators $\hat{A}$ through use of the classical-quantum correspondence [21]. We would rather work with operators that operate in the frequency domain, and we therefore make use of the Fourier transform,

$$\hat{A}_{\rightleftharpoons}(\omega) = \frac{1}{\sqrt{2\pi}} \int_{-\infty}^{+\infty} \hat{A}_{\rightleftharpoons}(x = 0, \tau) e^{i\omega\tau} \, d\tau. \tag{4.2}$$

These are non-Hermitian operators that satisfy

$$\hat{A}_{\rightleftharpoons}(\omega)^{\dagger} = \hat{A}_{\rightleftharpoons}(-\omega). \tag{4.3}$$

Using these operators, the Hamiltonian for the transmission line will then look like [21]

$$\hat{H} = \sum_{\sigma = \rightleftharpoons} \int_{-\infty}^{+\infty} \hat{A}_{\rightleftharpoons}(\omega) \hat{A}_{\rightleftharpoons}(-\omega) \, d\omega. \tag{4.4}$$

However, we would rather work with the usual annihilation and creation operators, which relate to the wave amplitude operators $\hat{A}$ as

$$\begin{aligned}\hat{a}_{\rightarrow}(\omega) &= \frac{\hat{A}_{\rightarrow}(\omega)}{\sqrt{\hbar|\omega|/2}} = \hat{a}_{\rightarrow}(-\omega)^{\dagger}\\ \hat{a}_{\leftarrow}(\omega) &= \frac{\hat{A}_{\leftarrow}(\omega)}{\sqrt{\hbar|\omega|/2}} = \hat{a}_{\leftarrow}(-\omega)^{\dagger}.\end{aligned} \tag{4.5}$$

After this quick motivation to why we can use creation and annihilation operators to quantize the field in a transmission line, we now turn our attention back towards the initial setup described in the beginning of this section. Exchanging $\rightleftharpoons$ for L/R and naming the operators of the left and right transmission lines as $\hat{a}$ and $\hat{b}$, the Hamiltonian of the right transmission line will take the form

$$\hat{H} = \int_0^{\infty} d\omega\hbar\omega\left[\hat{b}_R^{\dagger}\hat{b}_R + \hat{b}_L^{\dagger}\hat{b}_L\right], \tag{4.6}$$

and similarly but with operators a for the left transmission line. The $a_{R/L}$ and $b_{R/L}$ operators are defined in Fig. 4.1b. Since the transmission line is semi-infinite, the frequencies are continuos, and an integral is thus needed to account for the full energy of the system.

Current and voltage for the two travelling waves can generally be expressed as Hermitian operators of the form

$$\begin{aligned}\hat{V}^{\rightleftharpoons}(x,t) &= \sqrt{Z_c}\hat{A}^{\rightleftharpoons} = \sqrt{\frac{\hbar Z_c}{4\pi}}\int_{-\infty}^{\infty} d\omega\sqrt{|\omega|}\hat{a}^{\rightleftharpoons}(\omega)e^{-i\omega(t\mp x/v_p)}\\ \hat{I}^{\rightleftharpoons}(x,t) &= \frac{1}{\sqrt{Z_c}}\hat{A}^{\rightleftharpoons} = \sqrt{\frac{\hbar}{4\pi Z_c}}\int_{-\infty}^{\infty} d\omega\sqrt{|\omega|}\hat{a}^{\rightleftharpoons}(\omega)e^{-i\omega(t\mp x/v_p)},\end{aligned} \tag{4.7}$$

where v_p is the propagation velocity and Eq. (4.5) and the inverse Fourier transform has been used to define $\hat{V}$ and $\hat{I}$ from the annihilation operators [21]. For the setup considered here, the boundary condition at $x = 0$ can then be expressed using Kirchoff's circuit law which for current reads [22]

$$\begin{aligned}\sqrt{\frac{\hbar}{4\pi Z_0}}\int_{-\infty}^{\infty} d\omega\sqrt{|\omega|}(\hat{a}_R - \hat{a}_L)e^{-i\omega(t\mp x/v_p)} &= \sqrt{\frac{\hbar}{4\pi R}}\int_{-\infty}^{\infty} d\omega\sqrt{|\omega|}(\hat{b}_R - \hat{b}_L)e^{-i\omega(t\mp x/v_p)}\\ \implies \frac{1}{\sqrt{Z_0}}(\hat{a}_R - \hat{a}_L) &= \frac{1}{\sqrt{R}}(\hat{b}_R - \hat{b}_L),\end{aligned} \tag{4.8}$$

where we have assumed $\omega \neq 0$ and used the uniqueness of the Fourier transform to remove the integral. The boundary condition for voltage can be treated in a similar manner using Kirchoff's voltage law, which yields

$$\sqrt{Z_0}(\hat{a}_L + \hat{a}_R) = \sqrt{R}(\hat{b}_L + \hat{b}_R). \tag{4.9}$$

We now seek to determine how much of the left moving wave that is transmitted at $x = 0$, i.e.

$$\hat{a}_L = t(\omega)\hat{b}_L, \tag{4.10}$$

and we will assume that no photon is arriving from the right, meaning $\hat{a}_R = 0$. Rearranging and substituting from Eq. (4.8) and Eq. (4.9) then yields

$$t(\omega) = \frac{\sqrt{4RZ_0}}{R + Z_0} \implies |t(\omega)|^2 = \frac{4RZ_0}{(R + Z_0)^2}. \tag{4.11}$$

This is the usual transmission coefficient for impedance matching in microwave engineering, as was mentioned in Section 2.3.

The power leaving the resistor will then equal the number of photons at a given energy times the energy that each photon carries

$$P_{\mathrm{JN}}^{\leftarrow}(\omega) = \left\langle \hbar\omega \hat{a}_L^{\dagger} \hat{a}_L \right\rangle = |t(\omega)|^2 \hbar\omega \left\langle \hat{b}_L^{\dagger} \hat{b}_L \right\rangle = |t(\omega)|^2 \hbar\omega \frac{1}{e^{\frac{\hbar\omega}{k_B T_R}} - 1}, \tag{4.12}$$

where T_R is the temperature of the resistor. Due to symmetry, power will also be flowing from the transmission line with temperature T_L towards the resistor,

$$P_{\mathrm{JN}}^{\rightarrow}(\omega) = |t(\omega)|^2 \hbar\omega \frac{1}{e^{\frac{\hbar\omega}{k_B T_L}} - 1}, \tag{4.13}$$

and hence the net power leaving the resistor, $P_{\mathrm{JN}}(\omega)$, over the measurement bandwidth Δf is then

$$P_{\mathrm{JN}} = |t(\omega)|^2 \int_{\Delta f} \frac{d\omega}{2\pi} \hbar\omega \left(\frac{1}{e^{\frac{\hbar\omega}{k_B T_R}} - 1} - \frac{1}{e^{\frac{\hbar\omega}{k_B T_L}} - 1} \right). \tag{4.14}$$

Since the power P_{JN} varies slowly with frequency it can be assumed to be approximately constant over the measurement bandwidth ($\Delta f \approx 100$ MHz). Assuming f to be a frequency at the middle of the bandwidth, Eq. (4.14) then simplifies to

$$P_{\mathrm{JN}} = \frac{4RZ_0}{(R+Z_0)^2} hf\Delta f \left(\frac{1}{e^{\frac{hf}{k_B T_R}} - 1} - \frac{1}{e^{\frac{hf}{k_B T_L}} - 1} \right), \tag{4.15}$$

where a change of variable from angular frequency to bare frequency has also been performed.

Let's now consider the low frequency limit, where $k_B T_R \gg hf$. Using Taylor expansion, $e^x \approx 1 + x$, and assuming the resistive component is matched to the environment i.e. $\frac{4RZ_0}{(R+Z_0)^2} = 1$, yields simply

$$P_{\mathrm{JN}} = \Delta f k_B T_R, \tag{4.16}$$

where we now have recovered the noise power given by the voltage noise presented in [5]. This formula is useful to calculate the noise temperature of active components such as amplifiers, whose noise typically are in the classic regime.

4.2 Unity absorption

A necessary criteria to be able to measure close to unity emission is that the resistor is well matched to the rest of the measurement setup, since we want $|t(\omega)|^2 \approx 1$ in Eq. (4.14). Since the cables and components of the microwave lines typically have a characteristic impedance of 50 Ω, and we thus also want the resistor on the device, i.e. the copper island, to have a resistance close to this value. In Section 2.3 the resistance of the copper island was measured to be $R = 92$ Ω, which should yield an absorption/emission coefficient around $|t(\omega)|^2$=91%. However, this resistance was measured using dc signals, while the absorption and emission will be in the form of microwave signals. We should therefore also measure the absorption efficiency of these signals to confirm that it is close to unity.

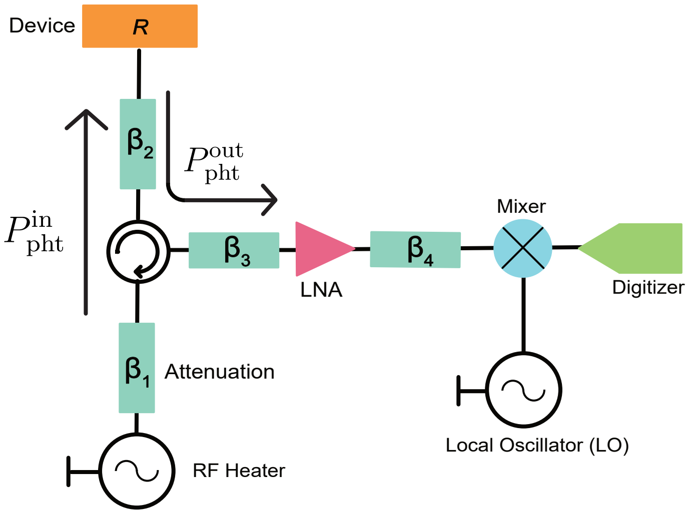

Figure 4.2: Measurement setup for the emission measurements. The device with resistance R can be heated with an ingoing microwave signal $P_{\mathrm{pht}}^{\mathrm{in}}$ generated from the RF source called RF heater. A microwave signal $P_{\mathrm{pht}}^{\mathrm{out}}$ is either reflected or emitted from the device, and will pass through both attenuation and amplification stages before reaching the mixer. The emitted signal is mixed with the signal from the Local Oscillator, which creates a signal with a frequency in the range that the digitizer can sample. The four general locations of attenuation along the microwave lines are named $\beta_1 - \beta_4$.

4.2.1 Measurement setup

Instead of directly measuring the absorption it is easier to measure reflected power Γ, and then infer the absorption efficiency as $|t(\omega)|^2 = 1 - \Gamma$. This measurement is performed by sending in a coherent microwave tone of a certain frequency f_x, and measuring the signal reflected back from the device. A simplified schematic of the measurement setup is shown in Fig. 4.2.

To measure the reflected signal, we utilize a setup with an RF-generator, acting as the local oscillator, set to a frequency f_{LO}. Our goal is to measure the reflected signal between the frequencies $4 - 8$ GHz, which is significantly higher than what the digitizer can sample. Therefore, the signal must be mixed down before reaching the digitizer. If the local oscillator frequency is set as $f_{\mathrm{LO}} = f_x + f_{\mathrm{if}}$, where f_{x} is a frequency of interest in the GHz regime and the intermediate frequency f_{if} is typically on the order of MHz (comparable to the sampling speed of the digitizer), a signal with frequency f_x will have a frequency $f_{\mathrm{LO}} - f_x = f_{\mathrm{if}}$ after mixing. This frequency is then of low enough frequency so that it can be sampled with the digitizer.

4.2.2 Quadrature sampling

The outgoing signal is sampled after mixing using quadrature sampling, or IQ sampling, which samples the in-phase (I) and quadrature (Q) components of a signal separately. It uses the fact that any sinusoidal signal can be written as a sum of two quadratures:

$$A\sin(2\pi ft+\phi)=\underbrace{A\cos(\phi)}_{I}\sin(2\pi ft)+\underbrace{A\sin(\phi)}_{Q}\cos(2\pi ft). \tag{4.17}$$

The amplitude of the signal can then be defined in the I-Q plane with radius $A^2 = I^2+Q^2$ and angle $\tan(\phi) = Q/I$.

The sampling of a pure sinusoidal signal is shown in Fig. 4.6a. The two quadratures are found by using a sampling frequency $f_S = 4f_{\text{if}}$, which samples at the times $t_n = n/f_S$, where n is an integer. Hence, 4 sample points s_n, with a 90 degree phase shift, are captured each period and the I and Q quadratures can then be found as

$$\begin{aligned} X_1 &= (s_0 - s_2)/2 = \frac{A}{2}(\sin(\phi) - \sin(\pi+\phi) = A\sin(\phi) = Q \\ X_2 &= (s_1 - s_3)/2 = \frac{A}{2}\left(\sin\left(\frac{\pi}{2}+\phi\right) - \sin\left(\frac{3\pi}{2}+\phi\right)\right) = A\cos(\phi) = I, \end{aligned} \tag{4.18}$$

from which the amplitude A and phase ϕ are reconstructed. This sampling scheme is insensitive to dc offsets and symmetric noise components.

The sampled signal amplitude A yields the voltage amplitude. The outgoing power $P_{\text{out}}^{\text{pht}}$ is then obtained as $P_{\text{out}}^{\text{pht}} = \frac{A^2}{2}$. To avoid contribution from the amplifier noise, the quadrature signals are averaged over several periods of frequency f_{if}.

4.2.3 Absorption efficiency

The inferred absorption efficiency from the reflection measurement is shown in Fig. 4.3. The measurement was performed by sweeping the frequency and measuring the reflected signal strength, both with the device loaded ($P_{\text{ref}}^{\text{device}}$) and unloaded ($P_{\text{ref}}^{\text{unloaded}}$). When the sample is unloaded, the impedance is effectively approaching ∞, which means that the signal should be perfectly reflected. By then comparing this value to the measured reflected signal power when the device is connected, $P_{\text{ref}}^{\text{device}}$, we can estimate the absorption A in the device as

$$|t(\omega)| = 1 - \frac{P_{\text{ref}}^{\text{device}}}{P_{\text{ref}}^{\text{unloaded}}}. \tag{4.19}$$

By comparing these two similar measurements on the same setup, differing only in whether the device is loaded, the absorption becomes independent of the attenuation and gain on the microwave lines.

The absorption efficiency is 95% on average over the measured 4-8 GHz band, with even the lowest efficiency being larger than 75%. Therefore, the overall absorption is close to unity. The peaks reaching a 100% absorption in Fig. 4.3 are most likely an artifact of interference, and power being absorbed at other parts of the lines than the device. At 5 GHz, the absorption is around 97% while we measure 95% absorption at 7.5 GHz. These frequencies are of particular interest as it is around these that the emission will be studied. A difference of 100% compared to 95% equals a difference of 0.22 dB. As we will see in Section 4.3.5, this is small in comparison to the uncertainty of the line gain, and it should therefore be safe to assume that all the ingoing power is absorbed by the device. Since

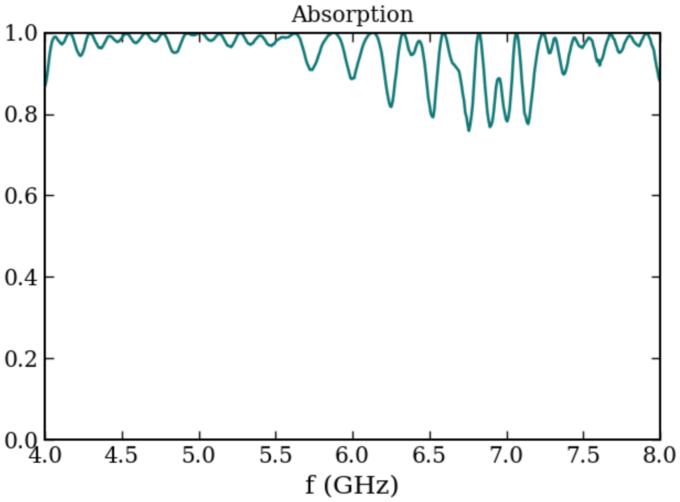

Figure 4.3: Absorption efficiency. Measured as the ratio of the signal strength that is reflected when the device is connected compared to when it is disconnected. The peaks reaching 100% absorption are an artifact of interference.

the absorption and emission efficiency are equal, the device should thus be able to achieve close to unity emission.

4.3 The art of measuring noise

Having established that the device exhibits an emission efficiency close to unity, we now shift our focus to the quantitative measurement of thermal noise. While the measurement setup and sampling method remain the same as to those described in Section 4.2.3, the transition from measuring a reflected coherent signal to stochastic emission requires a different analytical approach. Instead of tracking a single-frequency signal with a fixed phase, we must now characterize a signal with a constant power spectral density (PSD) and random phase.

4.3.1 Characterizing the stochastic emission signal

The ingoing microwave line can be used to send in a coherent signal of photons toward the copper island. These photons are absorbed with near 100% efficiency, (Fig. 4.3), and their energy, hf, is converted into heat. This thermalized energy can be re-emitted as thermal radiation. However, unlike the input signal, these emitted photons are no longer coherent as they instead follow a thermal distribution, as described by the quantum Johnson-Nyquist formula in Eq. (4.12). This emitted signal travels through the outgoing line and undergoes several stages of amplification before reaching the digitizer, where it is recorded as voltage fluctuations, $\langle V^2 \rangle$.

White noise and statistical distribtions

In the classical limit, Johnson-Nyquist noise exhibits a constant PSD (Eq. (4.16)), which is the defining characteristic of "white noise". While the quantum-limited PSD varies according to Eq. (4.12), it remains approximately constant over our specific measurement bandwidth $\Delta f_{BW} = 100$ MHz . Such a signal is referred to as locally white noise. A key property of white noise is that it is uncorrelated in time with an expectation value of $\langle V \rangle = 0$ [23].

The voltage measured at the digitizer will be the result of voltage fluctuations, which is described by the variance $\left\langle V^2 \right\rangle$. Since $\langle V \rangle = 0$, the total voltage fluctuations are equivalent to the variance (σ^2) of the sampled distribution:

$$\sigma^2 = \langle V^2 \rangle - \langle V \rangle^2 = \langle V^2 \rangle. \tag{4.20}$$

To capture these fluctuations accurately, we determine the I and Q components within one intermediate frequency period. This allows us to measure the voltage fluctuations on a timescale of $1/f_{IF}$. By collecting these sampled voltage points into a histogram, we can fit them with a Gaussian distribution [24] to extract the variance $\langle V^2 \rangle$.

The main challenge in this measurement is that the amplifiers contribute a massive amount of background noise that completely dominates the small thermal signal from the device. This is illustrated by the IQ histograms in Fig. 4.4. Fig. 4.4a shows the background noise with no heating applied, while Fig. 4.4b shows the distribution when the copper island is heated to $T_{NIS} = 160$ mK. Because the amplifier noise is so dominant, these two panels look completely identical to the naked eye. However, by subtracting the unheated background data from the heated data, we can isolate the true signal. The resulting difference is shown in Fig. 4.4, which reveals a clear emission signal and proves that we can successfully distinguish the thermal signal from the amplifier noise.

From measured voltage to emitted power

Once the background noise has been subtracted, the isolated voltage fluctuations can be translated into the actual physical power emitted by the device. The measured power at the digitizer is given by:

$$P_{\text{noise}} = \frac{\left\langle V^2 \right\rangle}{R}. \tag{4.21}$$

To find the actual power emitted at the device level (P_{JN}), we must scale this measured power to account for the total amplification and attenuation of the line

$$P_{\text{JN}} = 10^{-\beta/10}(P_{\text{meas}} - P_{\text{bkg}}), \tag{4.22}$$

where P_{bkg} is the power calculated from the unheated background fluctuations, and β represents the total line gain (in dB) between the device and the digitizer. The precise calibration of this line gain value β is described in detail in Section 4.3.7.

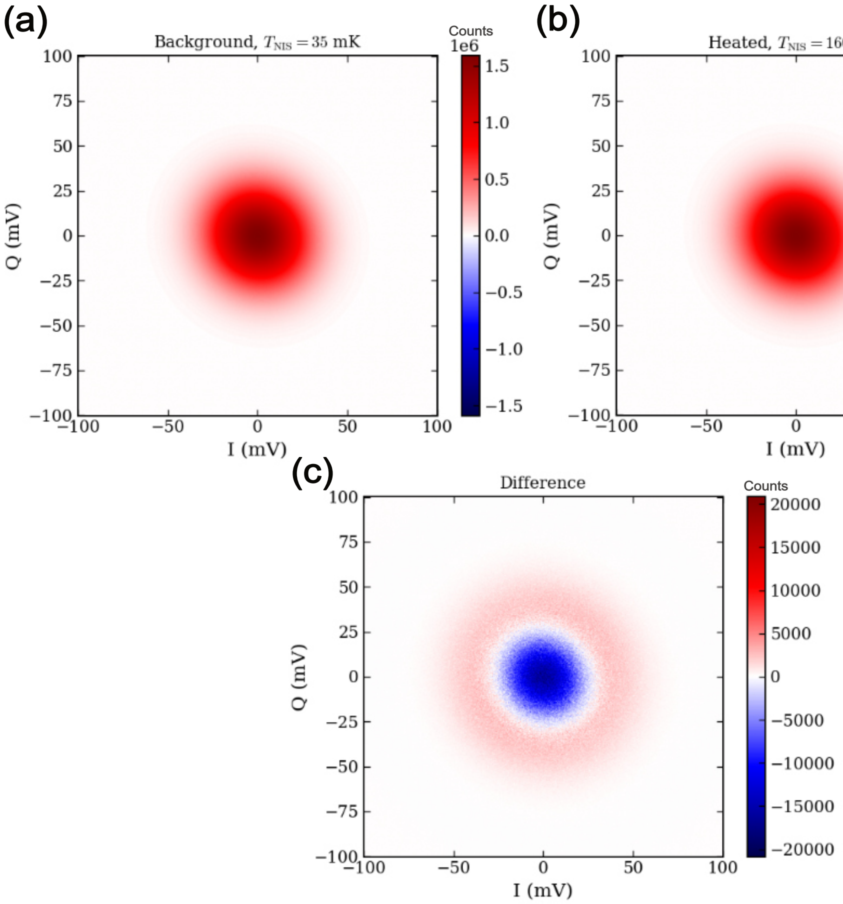

Figure 4.4: IQ histograms of the measured voltage at the digitizer, showing the voltage fluctuations originating from the device. The colorbar shows the number of counts. (a) Background, without any applied heating. (b) With the copper island heated to $T_{\rm NIS} = 160$ mK. (c) The difference between these two measurements.

4.3.2 Mixing and bandwidth

Before the digitizer can record the voltage fluctuations discussed in the previous section, the emitted high-frequency signal must be translated to a lower frequency, just as in the case of the reflected coherent signal in Section 4.2.3. This process is described in Fig. 4.5a. If the local oscillator frequency is set as $f_{\rm LO} = f_{\rm x} + f_{\rm if}$, where $f_{\rm x}$ is a frequency of interest in the GHz regime and the intermediate frequency $f_{\rm if}$ is typically on the order of MHz (comparable to the sampling speed of the digitizer), a signal with frequency f_x will have a frequency $f_{\rm if} = f_{\rm LO} - f_x$ after mixing. Similarly, a signal with frequency $f_y = f_{\rm x} + 2f_{\rm if}$ will mix down to $f_{\rm LO} - f_y = -f_{\rm if}$. Since $A\sin(-x) = -A\sin(x)$, this means that two different high-frequency signals, f_x and f_y, both end up at the exact same intermediate frequency $f_{\rm if}$. As a result, the power from both frequencies adds together at the digitizer. Because the noise has a constant PSD, both signals contribute the same amount of power, which doubles the measured PSD within the analogue bandwidth $\Delta f_{\rm BW}$. This can be seen as a doubling of the effective bandwidth. The actual noise frequencies captured with this setup are illustrated in Fig. 4.5b, where the doubled bandwidth, symmetric around $f_{\rm LO}$, is displayed.

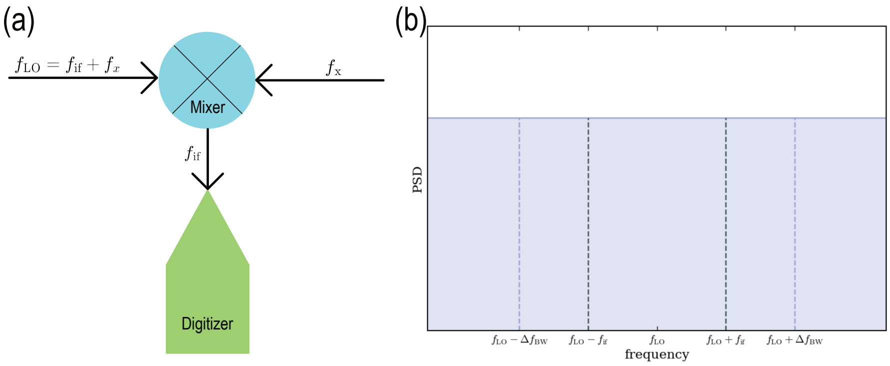

Figure 4.5: Explanation of the mixing process. (a) Illustration of the mixing process. The signal frequency f_x is mixed down with the local oscillator frequency f_{LO}, which results in a signal with the frequency f_{IF} leaving the mixer. (b) The (locally) constant PSD of Johnson-Nyquist noise, showing the doubled bandwidth, $f_{\mathrm{LO}} - \Delta f_{\mathrm{BW}}$ to $f_{\mathrm{LO}} + \Delta f_{\mathrm{BW}}$ that will be measured by the digitizer.

In the measurement setup used for the experiments, the analogue bandwidth is around $\Delta f_{BW} = 100$ MHz. The sampling frequency is typically chosen to be at least twice the analogue bandwidth, i.e. the Nyquist frequency, to avoid any aliasing effects. We have thus chosen $f_S = 200$ MHz, yielding $f_{\mathrm{if}} = 50$ MHz. We measure emission at $f_x = 5$ GHz and $f_x = 7.5$ GHz giving $f_{\mathrm{LO}} = 5.05$ GHz and $f_{\mathrm{LO}} = 7.55$ GHz. The emission is thus measured between the frequencies $4.95 - 5.15$ GHz and $7.45 - 7.65$ GHz.

4.3.3 Quadrature sampling of an emission signal

Fig. 4.6a and b shows IQ sampling of an signal with frequency $f = f_{\mathrm{if}}$ and $f = 2f_{\mathrm{if}}$ respectively. The four point IQ sampling described in Section 4.2.2 yields the correct amplitude for the signal frequency $f = f_{\mathrm{LO}} \pm f_{\mathrm{if}}$. The noise signal has however all the other frequencies nearby as well. We therefore need to consider what the measurement result for $f \neq f_{\mathrm{LO}} + f_{\mathrm{if}}$ will be.

While considering the IQ sampling of thermal noise we describe it as a signal $S = A\sin(2\pi ft + \phi)$ with a random amplitude A and a phase ϕ uniformly distributed over $[0, 2\pi]$. In describing the fluctuations as a random sinusoidal we are essentially abandoning the white noise description used earlier in Section 4.3.1. The variance of this sinusoidal signal is $\mathrm{V}[S] = \frac{1}{2}\mathrm{E}[A^2] = \frac{1}{2}(\mathrm{E}[I^2] + \mathrm{E}[Q^2])$ [23]. This is equal to defining the RMS-voltage as $V/\sqrt{2}$ as is typically done for a sinusoidal signal.

Derivation of the sampling attenuation

To estimate how much of the emission signal that is effectively measured with IQ sampling, we calculate the attenuation for a specific signal frequency f. A general signal of arbitrary frequency f can be written as $A\sin(2\pi ft + \phi)$ and the four samples s_n is sampled at the times $t_n = n/f_S = n/(4f_{\text{if}})$. The amplitude obtained with IQ-sampling is then:

$$\begin{aligned} X_1 &= (s_0 - s_2)/2 = \frac{A}{2}\left(\sin(\phi) - \sin\left(\frac{\pi f}{f_{\text{if}}} + \phi\right)\right) = -A\sin\left(\frac{\delta}{2}\right)\cos\left(\frac{\delta}{2} + \phi\right) \\ X_2 &= (s_1 - s_3)/2 = \frac{A}{2}\left(\sin\left(\frac{\pi f}{2f_{\text{if}}} + \phi\right) - \sin\left(\frac{3\pi f}{2f_{\text{if}}} + \phi\right)\right) = -A\sin\left(\frac{\delta}{2}\right)\cos(\delta + \phi), \end{aligned} \tag{4.23}$$

where $\frac{\delta}{2} = \frac{\pi f}{2f_{if}}$ and the trigonometric identity $\sin a - \sin b = 2\sin\left(\frac{a-b}{2}\right)\cos\left(\frac{a+b}{2}\right)$ has been used. The total measured squared amplitude will then be

$$A^2_{\text{meas}} = X_1^2 + X_2^2 = A^2\sin^2\left(\frac{\delta}{2}\right)\left(\cos\left(\frac{\delta}{2} + \phi\right) + \cos(\delta + \phi)\right), \tag{4.24}$$

which will depend on the phase of the signal. The used measurement scheme determines A_{meas} over several intermediate frequency periods. This corresponds to taking an average over all the phases ϕ, as the phase is randomly varying for a thermal signal. The average measured power can then be estimated by averaging over all phases ϕ:

$$A^2_{\text{avg}} = \frac{1}{2\pi}\int_0^{2\pi} A^2_{\text{meas}} d\phi = \frac{A^2}{2}(1 - \cos(\delta)) = \frac{A^2}{2}\left(1 - \cos\left(\frac{\pi f}{f_{\text{if}}}\right)\right). \tag{4.25}$$

The result is plotted in Fig. 4.6c. The signal frequency will thus affect the size of the measured amplitude when IQ sampling is used. The measured amplitude of the signal with frequency $f = 0$ or $f = 2f_{\text{if}}$ will for example equal zero, while A_{avg}=A for $f = f_{\text{if}}$.

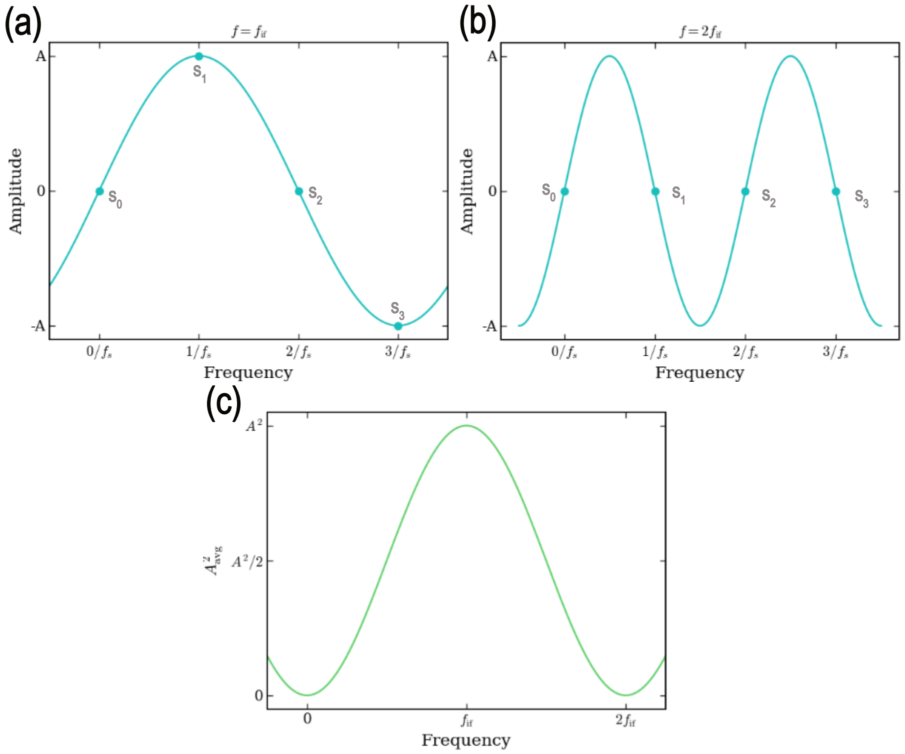

Figure 4.6: IQ sampling of an emission signal. (a) IQ sampling in the ideal case, with the signal frequency $f = f_{\text{if}}$ (b) IQ sampling of a signal with the frequency $f = 2f_{\text{if}}$. (c) A^2_{avg} from Eq. (4.24) as a function of frequency after mixing.

We can assume the amplitude of the emission signal to be more or less constant for the frequencies that are within the bandwidth of the oscilloscope after mixing, since the PSD is locally constant. We can then calculate the effective bandwidth of our measurements

$$\Delta f_{\text{eff}} = \frac{1}{2}\int_{-\Delta f_{BW}}^{\Delta f_{BW}} \left(1 - \cos\left(\frac{\pi f}{f_{\text{if}}}\right)\right) df = \left(\Delta f_{\text{BW}} - \frac{f_{\text{if}}}{\pi}\sin\left(\frac{\pi \Delta f_{\text{BW}}}{f_{\text{if}}}\right)\right), \tag{4.26}$$

which yields $\Delta f_{\text{eff}} = 100$ MHz for our particular setup.

4.3.4 Sampling from a statistical perspective

Instead of viewing the sampling of noise by considering the noise as a random sinusoidal signal as done above, we can choose to view it from a more statistical perspective. Each voltage sampled by the digitizer v_i can then be seen as a sample point from a Gaussian distribution $v_i \in \mathcal{N}(0, \sigma)$. The voltage fluctuation, i.e., the variance of the sampled signal, is calculated as

$$\sigma^2 = \left\langle V^2 \right\rangle = \frac{1}{n}\sum_{i=0}^{n-1}\left\langle v_i^2 \right\rangle . \tag{4.27}$$

The measured noise power at the digitizer can then be extracted as $P_n = \frac{\langle V^2 \rangle}{R}$. Because this direct statistical approach treats every sample point uniformly, it does not introduce the frequency-dependent filtering inherent to the four-point IQ scheme. Consequently, the signal is measured evenly across the entire downconverted spectrum, meaning the relevant bandwidth is simply the full doubled bandwidth after mixing, $2\Delta f_{\text{BW}} = 200$ MHz.

It is straightforward to show that from a statistical perspective, quadrature sampling is mathematically identical to this direct variance calculation. Assuming the same sampled points v_i, the sum of the variances of the I and Q quadratures is:

$$\begin{aligned}
\left\langle V_Q^2 \right\rangle + \left\langle V_I^2 \right\rangle &= \frac{4}{n}\sum_{i=4n}^{(n-1)/4}\left\langle \left(\frac{v_i - v_{i+2}}{2}\right)^2 \right\rangle + \frac{4}{n}\sum_{i=4n}^{(n-1)/4}\left\langle \left(\frac{v_{i+1} - v_{i+3}}{2}\right)^2 \right\rangle \\
&= \frac{4}{n}\sum_{i=4n}^{(n-1)/4}\left(\frac{\left\langle v_i^2 \right\rangle}{4} + \frac{\left\langle v_{i+1}^2 \right\rangle}{4} + \frac{\left\langle v_{i+2}^2 \right\rangle}{4} + \frac{\left\langle v_{i+3}^2 \right\rangle}{4}\right) \\
&= \frac{1}{n}\sum_{i=0}^{n-1}\left\langle v_i^2 \right\rangle = \sigma^2,
\end{aligned} \tag{4.28}$$

where we use the property that the covariance between two separate samples of white noise is zero. This proof demonstrates that looking at the data as a collection of Gaussian distributed points yields the exact same total variance σ^2, confirming that the statistical interpretation naturally spans the full 200 MHz bandwidth. This should be compared to the effective bandwidth of 100 MHz, when the same samples are viewed as the result of an IQ sampled random sinusoidal signal.

This comparison resolves an important distinction between the signal-based and statistical interpretations. While the absolute measured power and the theoretical thermal power predicted by Eq. (4.14) scale differently because they rely on different bandwidths and power calculations, the ratio $P/\Delta f$ remains perfectly constant between them. Therefore, evaluating the emitted noise in terms of power spectral density $(P/\Delta f)$ is the most meaningful approach, as it ensures the results are independent of the chosen mathematical framework and directly reflect the physical properties of the emitter.

4.3.5 Determination of line gain and attenuation

The thermal noise emitted from the copper island passes through several amplifying and attenuating components before it is measured by the digitizer. However, since the quantity of interest is the power emitted from the device rather than the signal strength at the digitizer, we must determine the total amplification the signal experiences. There is no simple way to precisely measure the effect of every individual component, since for example the cable attenuation at room temperature is different from lower temperature and connecting several tens of components together may increase the total attenuation. Instead, one must piece together various distinct measurements to estimate the line attenuation. We will begin by collecting these different pieces of information in Section 4.3.5, before combining them to model the gain and attenuation of the ingoing and outgoing line in Section 4.3.6 and Section 4.3.7.

Tabulated values for line attenuation

To estimate the line gain on the ingoing and outgoing microwave lines, we can sum the tabulated gain for the different components at the relevant frequencies. The component locations can be divided into four relevant placements, which are shown in Fig. 4.2:

1. Components in the ingoing line (β_1)
2. Components in the place where both ingoing and outgoing signal passes (β_2)
3. Components in the outgoing line, before the LNA (β_3)
4. Components in the outgoing line, after the LNA (β_4)

Table 4.1 lists the values of the gain and attenuation at these 4 locations placements, for the frequencies 5 GHz and 7.5 GHz used in this thesis. A full list with all the individual components can be found in Appendix A.

Element	β_1	β_2	β_3	β_4
Gain at 5 GHz (dB)	-82.25	-1.51	-1.18	95.02
Gain at 7.5 GHz (dB)	-86.28	-1.94	-1.6	91.22

Table 4.1: Tabulated line gain/attenuation at 5 and 7.5 GHz, divided into the four different regions that are listed in Section 4.3.5 and shown in Fig. 2.1. The total line gain for the ingoing line is given as the sum of region 1 and 2, while the outgoing line is the sum of region 2, 3 and 4.

With the component values we obtain a rough estimate of the gain on the ingoing and outgoing microwave lines. Uncertainties in the specified gain arises due to that:

- Cable RT-4K and 4K-MXC (Appendix A) does not have a specified insertion loss at the relevant frequencies, in which case a linear interpolation has been performed to find an approximation. They also connect stages at different temperatures, and since the attenuation is temperature dependent this results in an uncertainty in attenuation. (β_1, β_4)

- There are two filters installed at 200 mK which is a lower temperature than what they are specified for. These are assumed to have the specified insertion loss also at these temperatures. (β_3)
- There is one cable (Blueforce Cu) with an unknown attenuation, assumed to be have the same attenuation as a similar cable (PE3W05577 Appendix A). (β_2)
- There may also be small individual variations between components.

These are all uncertainties of approximately a few dB at most, but since it is important to achieve as low uncertainty as possible, further calibration is needed. The tabulated values will however constitute a good starting point for the following calibration steps.

Reflected signal strength

The total gain on the lines can be measured by sending in a microwave signal with a specified power when the device is disconnected, which means that the full signal will be reflected. The reflected signal travels through the outgoing line and is then measured by the digitizer. By comparing the ingoing power with the measured power, the total gain on the lines can be determined.

Measurement of the reflected signal strength was first performed during unloading of the device, which meant that the cable located inside the probe was not included in the reflection measurement. The temperature during the measurement was also around 500 mK instead of the base temperature 10 mK. Later, the probe was loaded empty, without a device, to allow for measurements of the total line gain at base temperature, and with all components included. The data from these two measurements are shown in Fig. 4.7.

The difference in line gain between measuring the full setup and having the probe disconnected can be explained by the attenuation of the cable in the probe, which is only included in the full setup case. The tabulated component values predicts that this should add approximately -1 dB at 5 GHz and -1.4 dB at 7.5 GHz (see appendix A), which is in close correspondence with the measured difference in Fig. 4.7. Hence, the temperature difference between 500 mK instead of 10 mK does not seem to influence the cable attenuation.

The measured total gain in Fig. 4.7 can be compared to the total line gain from the tabulated values in Table 4.1. This comparison is summarized in Table 4.2. The measurement of the total line gain indicates that there should be 2.72 dB and 8.34 dB more attenuation at 5 and 7.5 GHz respectively, compared to what is tabulated in Table 4.1.

Frequency	**5 GHz**	**7.5 GHz**
Measured total line gain	6.85 dB	-8.87 dB
Total tabulated line gain	9.57 dB	-0.54 dB
Difference	**-2.72 dB**	**-8.34 dB**

Table 4.2: Comparison between total tabulated and total measured line gain at the two relevant frequencies. As is shown in Fig. 4.7 the measured line gain varies with frequency.

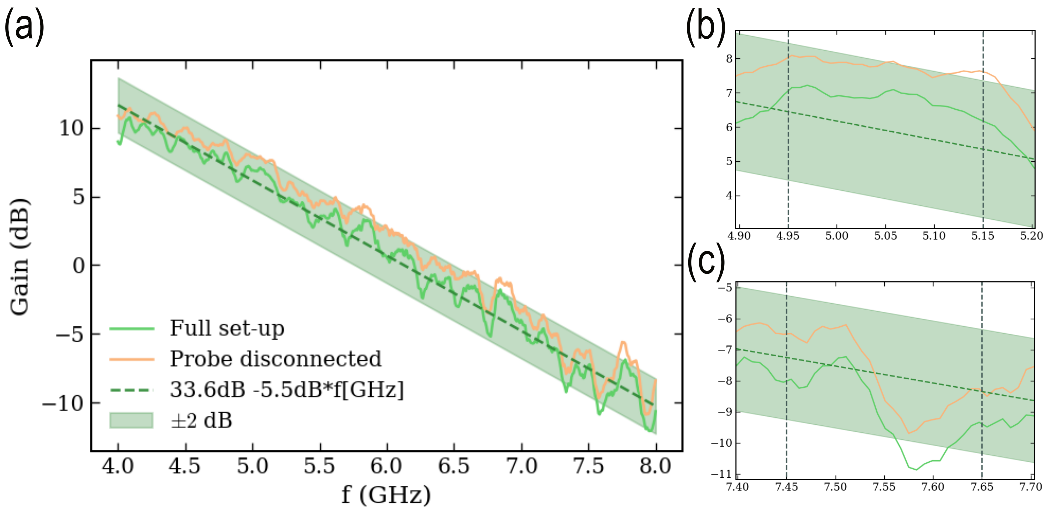

Figure 4.7: Total line gain, measured by sending in a power $P_{\text{in}} = -35$ dBm and measuring the reflected power P_{r} at the digitizer. The total line gain is then the difference between $P_{\text{r}} - P_{\text{in}}$. (a) Total line gain calculated over the full frequency range. The green line shows the line attenuation measured at base temperature when the probe was loaded empty, while the orange line shows the line gain when the probe is disconnected. The dashed line is a linear fit (in dB) to the green line. (b) and (c) shows the total line gain for the bandwidths given by $f_{\text{LO}} = 5.05$ GHz and $f_{\text{LO}} = 7.55$ GHz. The dashed grey lines marks the approximate start and end of the band.

Furthermore, the reflected signal strength has been measured for different setups during the course of the experiments. One interesting difference to study is what effect installation of the filters in the cryostat had. This comparison is shown in figure Fig. 4.8. Apart from adding filters to the outgoing line, the amplification after mixing was also changed from 40 dB to 20 dB between the setups, which has been accounted for in Fig. 4.8. According to the specifications, the filters add approximately 1.2 dB attenuation at 5 GHz and 1.6 dB at 7.5 GHz (see appendix A). Therefore, it is a bit surprising that we for some frequencies within the bandwidth located at 7.5 GHz measure less attenuation after installation of the filters. However, this may instead be attributed to impedance mismatches or standing waves, which could change the amplification more than the specified insertion loss.

4.3.6 Calibrating the ingoing line

A reference point to the calibration question is obtained by comparing the two complementary heating methods of the copper island, microwave absorption and Joule heating in the high bias regime. Joule heating was performed by applying a bias $V_h \gg \Delta$ to an NIS junction. The applied power to the island is then $V_h I_h/2$, as was described in Section 2.1.2. The ingoing microwave line can then be calibrated by assuming that the same applied power to the copper island ought to result in the same temperature increase. This calibration is seen in Fig. 4.9. To get the microwave heating to correspond to the Joule heating, 0.7 dB more attenuation is added to the tabulated values at 5 GHz and 2 dB at 7.5 GHz. This yields the total ingoing line gain $\beta_1 + \beta_2 = -84.46$ dB at 5 GHz

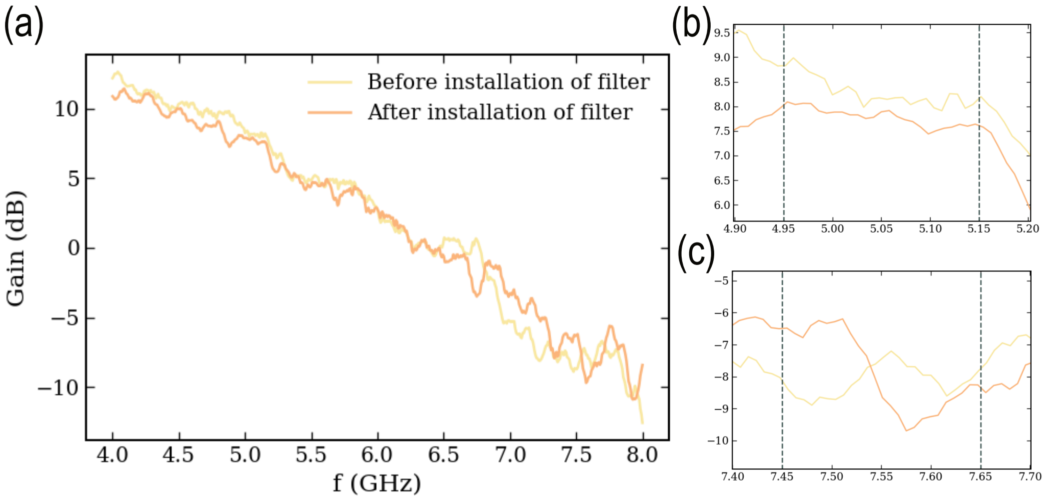

Figure 4.8: Total line gain, measured by sending in a power $P_{\text{in}} = -35$ dBm and measuring the reflected power P_{r} at the digitizer. The total line gain is then the difference between $P_{\text{r}} - P_{\text{in}}$. (a) Total line gain calculated over the full frequency range. The two lines show the measured total line gain before and after the filters were installed. The line gain before installing filters were measured with 20 dB more amplification, and 20 dB has therefore been subtracted to get comparable data. (b) and (c) shows the total line gain for the bandwidths given by $f_{\text{LO}} = 5.05$ GHz and $f_{\text{LO}} = 7.55$ GHz. The dashed grey lines marks the approximate start and end of the bands.

and $\beta_1 + \beta_2 = -90.22$ dB at 7.5 GHz. In this calibration we have assumed all the ingoing microwave power to be absorbed by the copper island, as was shown to be true within 95% for these two frequencies in Section 4.2.3.

4.3.7 Calibrating the outgoing line

The total line gain must be consistent with the values derived from the reflected signal strength. Consequently, any remaining difference in total gain budget after calibrating the ingoing line is attributed to the outgoing line. This corresponds to an additional 2 dB of attenuation at 5 GHz and 6.3 dB at 7.5 GHz. To determine if these values represent a physically realistic calibration, we can determine the noise temperature of the noise originating from the LNA. Comparing this value to the manufacturer's specifications verifies that our gain distribution after the LNA, β_4, is accurate.

Amplifier noise temperature

The Low Noise Amplifier (LNA), situated on the outgoing line at the 4K stage in the cryostat, has a specified noise temperature of close to 1.6 K at 5 GHz and around 2K at 7.5 GHz and is the main contributor to noise in the setup. This has been confirmed by comparing the measured noise when the amplifier is turned on and off, in which case the power measured at the digitizer when the LNA is turned off is only 5% of what is measured with the LNA turned on.

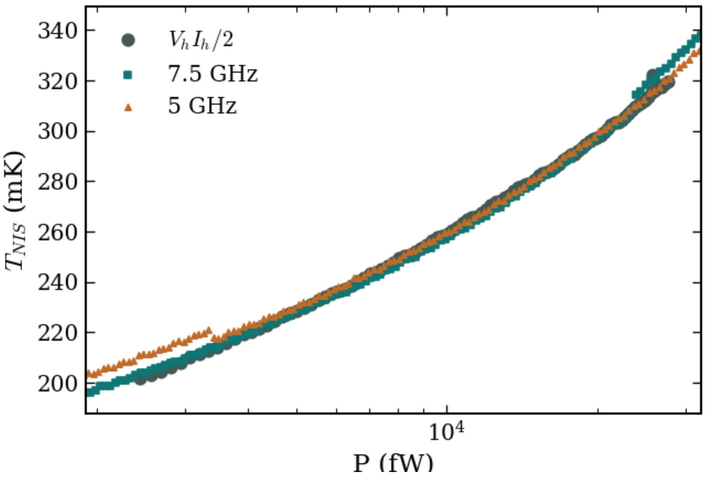

Figure 4.9: Calibration of the ingoing microwave line. The attenuation at 5 GHz is 84.46 dB and at 7.5 GHz 90.22 dB, which is 0.7 dB respectively 2 dB more than what is tabulated in Table 4.1.

The noise temperature for the LNA can be calculated from the measured background fluctuations in Fig. 4.4a, by use of Eq. (4.16) and the tabulated attenuation in Table 4.1 for the outgoing line from the LNA and onwards. Comparing that to the specified noise temperature, will give an indication of how well calibrated that part of the line is. At 5 GHz, the estimated noise temperature from the fluctuations is:

$$T_{\text{noise}}^{\text{5GHz}} = \frac{P_{noise}}{\Delta f k_B} = \frac{\left\langle V_{meas}^2 \right\rangle * 10^{-\beta_4}}{\Delta f k_B R} = 1.92\text{K},$$

while the temperature at 7.5 GHz instead is

$$T_{\text{noise}}^{\text{7.5GHz}} = 0.52\text{K}.$$

Both the noise temperatures T_{noise} have been calculated using the values $\Delta f = 200$ MHz and $R = 50\Omega$.

The noise temperature given by the tabulated attenuation in Table 4.1 is approximately 20% larger than what is specified for the LNA at 5 GHz. This corresponds to 0.8 dB more gain on the outgoing line from the LNA and onwards than what the tabulated values suggests. At 7.5 GHz, the discrepancy is larger, with a measured noise temperature of 26% of the specified value. To measure the specified noise temperature at 7.5 GHz, -5.9 dB less gain would need to be assumed on the outgoing line.

The total line gain needs to equal what was measured from the reflected signal strength. Therefore, the remaining difference in gain, after calibration of the ingoing line, should be located at the outgoing line. This gives 2 dB more attenuation at 5 GHz, and 6.3 dB more attenuation at 7.5 GHz. This is in close correspondence to the discrepancy in noise temperature at 7.5 GHz. At 5 GHz, we would like to assume that this extra attenuation is located before the LNA, as any more attenuation after the LNA would result in a higher measured noise temperature. We thus obtain $\beta_2 + \beta_3 + \beta_4 = 90.33$ dB of which the change $\Delta\beta_4 = 0$ dB at 5 GHz and $\beta_2 + \beta_3 + \beta_4 = 81.38$ dB of which the change $\Delta\beta_4 = -5.9$ dB at 7.5 GHz.

Final line gain estimation

The performed calibration indicates how the difference in gain between the tabulated and measured gain should be divided between the ingoing (β_1, β_2) and outgoing line (β_2, β_3, β_4), together with how much that should be placed after the LNA (β_4). This distribution is enough for the purpose of the measurements in this thesis, as it is only the total gain of the ingoing and outgoing line that is of interest. We therefore only specify the estimate of the total gain of the ingoing and outgoing line, which is shown in Table 4.3.

Element	Ingoing line ($\beta_1 + \beta_2$)	Outgoing line ($\beta_2 + \beta_3 + \beta_4$)
Tabulated gain at 5 GHz (dB)	-83.76	92.33
Final gain at 5 GHz (dB)	-84.46	90.33
Difference (dB)	-0.7	-2
Tabulated gain at 7.5 GHz (dB)	-88.22	-87.68
Final gain at 7.5 GHz (dB)	–90.22	81.38
Difference (dB)	-2	-6.3

Table 4.3: Tabulated and final line gain/attenuation at 5 and 7.5 GHz, divided into the ingoing and outgoing line.

4.3.8 Estimation of the calibration accuracy

Despite calibrating the ingoing and outgoing lines as carefully as possible, some uncertainties in the calibration remains. We use the approximate ±2 dB variations of the measured total line gain, illustrated in Fig. 4.7, as an estimate of the accuracy of the calibration method.

An additional source of measurement uncertainty arises from the analogue bandwidth. This parameter is difficult to pinpoint exactly. An increase of 25%, from an analogue bandwidth of 100 MHz to 125 MHz, could for example account for the discrepancy observed in the LNA noise temperature at 5 GHz. The assumed 100 MHz bandwidth merely represents the region where the filter's insertion loss is below 1 dB, which implies that a substantial amount of noise power still passes through the system outside of this band.

4.4 Thermal photoemission

4.4.1 Comparison of different heating methods

The measured emission in fW/MHz is shown in figure Fig. 4.10 for 5 GHz and Fig. 4.11 for 7.5 GHz. To measure the thermal photoemission as a function of temperature, the island is heated either by ingoing microwave photons or by applying a dc signal over an

NIS junction. For the microwave heating signals, the frequency is above or below the measurement band so that it does not interfere with the emission measurement. The different heating methods show the same response and depends only on the temperature of the copper island T_{NIS}. This is a strong indication that the emission is thermal, as the emission power is independent of the heating source and follows the island temperature.

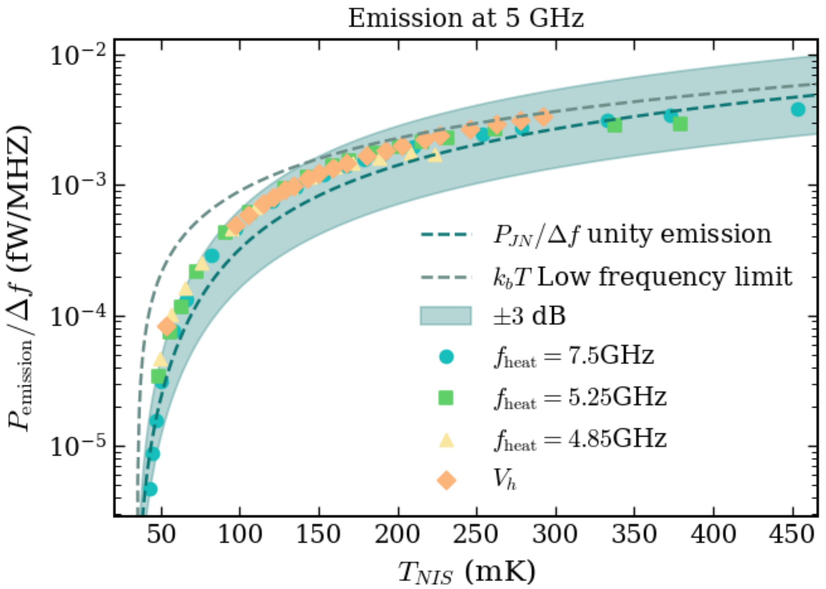

Figure 4.10: Measured emission (fW)/(MHz) at 5 GHz as a function of temperature T_{NIS}, for several different heating methods. The theoretical maximum unity emission (Eq. (4.15)) is plotted as a dashed line together with the low frequency limit (Eq. (4.16)) as a reference. The gray region indicates an area of ±3 dB around the dashed line denoting unity emission.

4.4.2 Unity emission

Fig. 4.10 and Fig. 4.11 show lines for the theoretical unity emission $P_{\text{JN}}/\Delta f$ (Eq. (4.15)) and the low-frequency approximation (Eq. (4.16)) as a reference, together with the measured emission. At 5 GHz (Fig. 4.10), the emission is within a factor of 1.5 of unity, and all of the data points fall within the ±3 dB area. At 7.5 GHz, the emission reaches 50% of the unity-emission limit. The experimental data captures the same functional shape and trend as the unity-emission curve at both frequencies. The emission measurements thus demonstrate the successful realization of a thermal photoemitter operating with near-unity efficiency, within an experimental uncertainty of approximately 50%. Furthermore, this effectively provides a direct measurement of photonic heat flow, as it is fundamentally equivalent to the Johnson-Nyquist noise described in Section 4.1.

This experimental uncertainty comes mostly from the line calibration rather than the device itself. Because the absorption efficiency was shown to be around 95% in the previous section, the actual physical emission is likely much closer to unity. The fact that the measured data captures the same shape as the theory line further shows that the underlying

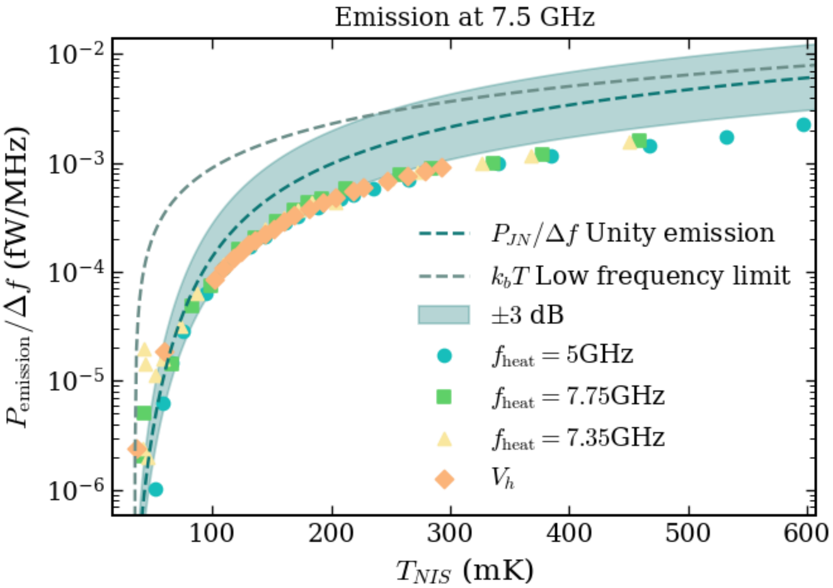

Figure 4.11: Measured emission (fw)/(MHz) at 7.5 GHz as a function of temperature T_{NIS}, for several different heating methods. The theoretical maximum unity emission (Eq. (4.15)) is plotted as a dashed line together with the low frequency limit (Eq. (4.16)) as a reference. The gray region indicates an area of ±3 dB around the dashed line denoting unity emission.

physics is correct. Therefore, the 50% uncertainty reflects the limits of the measurement setup rather than a flaw in the photoemitter itself.

Chapter 5

Heat flow and absorption

Up until this point, our analysis has focused on emission as a function of the island temperature, T_{NIS}. While the island has been heated using both microwave signals and a voltage-biased NIS junction, this heating has simply been treated as a means to maintain a specific temperature T_{NIS}. This chapter shifts focus to investigate the heat flow dynamics by examining how this applied heating power is distributed through the system. When energy is injected to heat the island, it escapes through two primary channels. It can dissipate into the substrate lattice via phonons, or it can be radiated away as photons through electron-photon coupling. This electron-photon coupling produces the emission signal we measured in Chapter 4.

The chapter begins by outlining the theory for electron-phonon and electron-photon coupling. We also discuss the superconductor's role as a thermal isolator. Following this theoretical framework, we present and characterize the experimental results, comparing them to a standard heat flow model. Finally, the measured heat flow is compared with similar structures from previous studies, including a discussion on how geometric differences might influence the heat flow.

5.1 Electron-phonon coupling

In a typical metal, heat is typically carried mainly by electrons. The electrons may also release their kinetic energy to the lattice, i.e. the phonons. At room temperature, the coupling between electrons and phonons is strong, which means that no temperature difference between the systems in general is generated. At lower temperatures however the coupling between electrons and phonons is much weaker, and as a consequence the two systems can be driven far out of thermal equilibrium. The two systems then obtain two different temperatures, the electron temperature T_e and the phonon temperature T_{phn} [25]. The temperature T_{NIS} probed by the NIS junction in previous experiments is the electronic temperature T_e. This section will derive the heat flow between electrons and phonons that arises due to this electron-phonon coupling at low temperatures. The derivation is based on Ref. [26], but carried out for the case of a normal metal instead of a superconductor.

To begin with, the full Hamiltonian of the system can be written as a sum of three Hamiltonians

$$H = H_e + H_{\text{phn}} + H_{\text{e-phn}}. \tag{5.1}$$

The energy of the electrons in the metal is described by H_e:

$$H_e = \sum_{k,\sigma} \epsilon_k c^\dagger_{k,\sigma} c_{k,\sigma}, \tag{5.2}$$

where $c^\dagger_k$ and c_k are fermionic creation and annihilation operators and $\epsilon_k = \frac{\hbar^2 k^2}{2m}$. Similarly, H_{phn} describes the phonon energy in the system as:

$$H_{\text{phn}} = \sum_q \hbar\omega_q (b^\dagger_q b_q + \frac{1}{2}), \tag{5.3}$$

where $b^\dagger_q$, b_q are bosonic operators and the factor 1/2 represents the zero point energy. The Hamiltonian for the electron-phonon interaction of the system is

$$H_{\text{e-phn}} = \sum_{k,q,\sigma} g_q \left(c^\dagger_{k,\sigma} c_{k-q,\sigma} b_q + c^\dagger_{k,\sigma} c_{k+q,\sigma} b^\dagger_q \right), \tag{5.4}$$

where $g_q = \nu\omega_q^{1/2}$ typically is taken to be the coupling factor between the systems and ν is a coupling constant [25]. The first term of the Hamiltonian represents an electron absorbing a phonon with momentum q while the second term instead represents an electron losing momentum q via emission of a phonon. The interaction and coupling between electrons and phonons can be viewed as a perturbation to the system.

The operator for the heat flux to the phonons can be found by taking the derivative of the phonon Hamiltonian,

$$\dot{H}_{\text{phn}} = \frac{i}{\hbar}[H, H_p] = \frac{i}{\hbar}[H_{\text{e-ph}}, H_p] = \nu\omega_q^{1/2} \sum_{k,q} \left(c^\dagger_k c_{k-q} b_q - c^\dagger_k c_{k+q} b^\dagger_q \right), \tag{5.5}$$

where we have used that H_e and H_{phn} commutes, together with commutator rules for fermionic and bosonic operators respectively. To calculate the expectation value for the heat flow operator the Kubo formula, which is an expression for the linear response of an observable quantity when disturbed by a small perturbation [14], can be used. In this case, the perturbation is described by $H_{\text{e-phn}}$, and the Kubo formula then reads:

$$\begin{aligned} \dot{Q}_{\text{e-phn}} = \langle \dot{H}_{\text{phn}} \rangle = \langle \dot{H}_{\text{phn}} \rangle_0 - \frac{i}{\hbar} \int_{-\infty}^{t} dt' \langle [\dot{H}_{\text{phn}}(t), H_{e-phn}(t')] \rangle_0 \\ = \frac{1}{\hbar}\nu^2 \sum_{k\sigma q} \sum_{k'\sigma'} \omega_q^2 \int_{-\infty}^{t} dt' \Big\{ \langle [c^\dagger_{k\sigma}(t) c_{k-q\sigma}(t) b_q(t), c^\dagger_{k'\sigma'}(t') c_{k'+q\sigma'}(t') b^\dagger_q(t')] \rangle_0 \\ - \langle [c^\dagger_{k\sigma}(t) c_{k+q\sigma}(t) b^\dagger_q(t), c^\dagger_{k'\sigma'}(t') c_{k'-q\sigma'}(t') b_q(t')] \rangle_0 \Big\}, \end{aligned} \tag{5.6}$$

where $\left\langle \dot{H}_{\text{phn}} \right\rangle_0$ denotes the expectation value evaluated with respect to the unperturbed state.The expression is simplified by noting that $\left\langle \dot{H}_{\text{phn}} \right\rangle_0 = 0$ and that only commutators containing operators that in total keeps the number of phonons conserved will have a non-zero expectation value.

The expectation value of the commutators can be evaluated in the Heisenberg picture, which factors out the time dependence as $b_q(t) = e^{-i\omega q} b_q$ and $b_q^\dagger(t) = e^{i\omega q} b_q^\dagger$ and similarly for the operators $c_q^\dagger(t)$ and $c_q(t)$. The first term in equation Eq. (5.6) can then be calculated as:

$$\begin{aligned}
& \langle [c_{k\sigma}^\dagger(t) c_{k-q\sigma}(t) b_q(t), c_{k'\sigma'}^\dagger(t') c_{k'+q\sigma'}(t') b_q^\dagger(t')] \rangle_0 = \\
= \; & e^{i\omega_q(t'-t)} e^{i(\epsilon_k t/\hbar - \epsilon_{k-q} t/\hbar + \epsilon_{k'} t' - \epsilon_{k'+q} t')} \langle [c_{k\sigma}^\dagger c_{k-q\sigma} b_q, c_{k'\sigma'}^\dagger c_{k'+q\sigma'} b_q^\dagger] \rangle_0 = \\
= \; & e^{i\omega_q(t'-t)} e^{i(\epsilon_{k-q} - \epsilon_k)(t'-t)/\hbar} \langle [c_{k\sigma}^\dagger c_{k-q\sigma} b_q, c_{k-q\sigma'}^\dagger c_{k\sigma'} b_q^\dagger] \rangle_0 = \\
= \; & e^{i\omega_q(t'-t)} e^{i(\epsilon_{k-q} - \epsilon_k)(t'-t)/\hbar} \left(f_k(1 - f_{k-q})(n_q + 1) - f_{k-q}(1 - f_k) n_q \right).
\end{aligned} \tag{5.7}$$

The operators have been paired as $k = k' + q$ and the expectation value was calculated by using that the fermionic number operators follow the Fermi distribution, i.e. $\left\langle c_k^\dagger c_k \right\rangle = f_k$, while the expectation value for a bosonic number operator instead follow the Bose-Einstein distribution as $\left\langle b_q^\dagger b_q \right\rangle = n_q$.

The second term in Eq. (5.6) can be calculated in a similar manner, and by pairing the operators with $k' = k + q$ and then changing the summation index from k' to k the expectation value becomes:

$$\begin{aligned}
& \langle [c_{k\sigma}^\dagger(t) c_{k+q\sigma}(t) b_q^\dagger(t), c_{k'\sigma'}^\dagger(t') c_{k'-q\sigma'}(t') b_q(t')] \rangle_0 = \\
= \; & e^{-i\omega_q(t'-t)} e^{-i(\epsilon_{k-q} - \epsilon_k)(t'-t)/\hbar} \left(f_{k-q}(1 - f_k) n_q - f_k(1 - f_{k-q})(n_q + 1) \right).
\end{aligned} \tag{5.8}$$

Next, the time integration in expression Eq. (5.6) can be performed to obtain energy conservation rules in the form of delta functions. To further simplify the expression, the sums can be replaced with integrals. For the sum over the phonon momentum q, this change looks like

$$\sum_q \to \frac{V}{(2\pi)^3} \int d^3 q, \tag{5.9}$$

where V is the volume of the metal and $\frac{V}{(2\pi)^3}$ is the phonon density of states (DOS) in a 3D bulk material. Similarly, the sum over electron momentum k can be approximated with an integral as:

$$\sum_{k,\sigma} \to \int d\epsilon_k N(\epsilon_k), \tag{5.10}$$

where a variable change $k \to \epsilon_k$ has also been performed to integrate over electron energies instead of electron momentum. $N(\epsilon_k)$ here accounts for the electron DOS. The final simplified expression after these three changes then reads:

$$\begin{aligned}
\dot{Q}_{\text{e-phn}} = 2\pi\nu^2 \frac{V}{(2\pi)^3} & \int_{-\infty}^{\infty} d\epsilon_k N(\epsilon_k) \int d^3 q \omega_q^2 \\
\times \quad & \left[\left(f_k(1 - f_{k-q})(n_q + 1) - f_{k-q}(1 - f_k) n_q \right) \delta(\hbar\omega_q - \epsilon_k + \epsilon_{k-q}) \right. \\
& \left. - \left(f_{k-q}(1 - f_k) n_q - f_k(1 - f_{k-q})(n_q + 1) \right) \delta(-\hbar\omega_q + \epsilon_k - \epsilon_{k-q}) \right].
\end{aligned} \tag{5.11}$$

From this expression two things can be noted:

1. Only electrons close to the Fermi energy E_f can absorb/emit phonons and therefore the electron DOS can be approximated as a constant, $N(\epsilon_k) \approx N(E_F)$, as it compared to the Fermi functions is slowly varying around E_F
2. By introducing standard spherical coordinates, $dq^3 = q^2 \sin\theta \, dq \, d\theta \, d\phi = q^2 \, dq \, d(\cos(\theta)) \, d\phi$ and let θ be the angel between the k and q vector, we obtain $\int_0^{2\pi} d\phi = 2\pi$. The energy difference between k and q then only depends on θ and not ϕ. Furthermore, by using the law of cosine the energy difference ϵ_{k-q} can be simplified as $\epsilon_{k-q} = \frac{\hbar^2|\mathbf{k}-\mathbf{q}|^2}{2m} = \frac{\hbar^2k^2}{2m} + \frac{\hbar^2q^2}{2m} - \frac{2kq\cos(\theta)}{2m} \approx \frac{\hbar^2k^2}{2m} - \frac{2kq\cos(\theta)}{2m}$ where the q^2 term is small in comparison and therefore neglected. The delta functions will then take the form $\delta(\pm(\hbar\omega_q - \frac{\hbar^2 kq\cos(\theta)}{m}))$. Integrating these over θ then yields $\int d\cos(\theta)\delta(\pm(\hbar\omega_q - \frac{\hbar^2 kq\cos(\theta)}{m}) = \frac{m}{qk\hbar^2} \approx \frac{m}{qk_F\hbar^2}$

Implementing these changes together with $\omega_q = c_l q$ where c_l is the speed of sound, yields the expression:

$$
\begin{aligned}
\dot{Q}_{\text{e-phn}} = {} & 2\pi\nu^2 \frac{V}{(2\pi)^3} N(E_F) \int_{-\infty}^{\infty} d\epsilon_k 2\pi \int_0^\infty dq q^2 c_l^2 q^2 \frac{m}{qk_F\hbar^2} \\
\times \quad & 2\left(f_k(1-f_{k-q})(n_q+1) - f_{k-q}(1-f_k)n_q\right) = \\
= {} & \frac{V\nu^2 c_l^2 m N(E_F)}{\pi k_F \hbar^2} \int_{-\infty}^{\infty} d\epsilon_k \int_0^\infty dq q^3 \left(f_k(1-f_{k-q})(n_q+1) - f_{k-q}(1-f_k)n_q\right).
\end{aligned}
\tag{5.12}
$$

Next, the integration variable q can be changed to $\epsilon = \hbar\omega_q = \hbar c_l q$ which give $dq = (\hbar c_l)^{-1} d\epsilon$. By also expanding and simplifying the remaining integrand, we obtain:

$$
\begin{aligned}
\dot{Q}_{\text{e-phn}} &= \frac{V\nu^2 m N(E_F)}{\pi c_l^2 k_F \hbar^6} \int_{-\infty}^{\infty} d\epsilon_k \int_0^\infty d\epsilon \epsilon^3 \left(f(\epsilon_k) - f(\epsilon_k - \epsilon))n(\epsilon) + f(\epsilon_k)(1 - f(\epsilon_k - \epsilon))\right) \\
&= \frac{V\nu^2 m N(E_F)}{\pi c_l^2 k_F \hbar^6} \int_{-\infty}^{\infty} d\epsilon_k (f(\epsilon_k) - f(\epsilon_k - \epsilon)) \int_0^\infty d\epsilon \epsilon^3 (n(\epsilon, T_e) - n(\epsilon, T_{phn}),
\end{aligned}
\tag{5.13}
$$

where for the last step we have used the identity $f(\epsilon_k)(1-f(\epsilon_k-\epsilon)) = n(\epsilon)(f(\epsilon_k-\epsilon)-f(\epsilon_k))$, which holds in thermal equilibrium between the fermions and bosons. The electron part of the integral can now easily be calculated as it is just the difference between two Fermi functions shifted by ϵ, and will thus equal ϵ. The phonon part is then calculated by making the variable change $x = \epsilon/(k_BT)$ and for each Bose-Einstein function the integral can then be calculated as

$$
\int_0^\infty d\epsilon \epsilon^4 n(\epsilon, T) = (k_BT)^5 \int_0^\infty \frac{x^4}{e^x - 1} dx = (k_B T^5) \cdot 24\zeta(5),
\tag{5.14}
$$

where $\zeta(5)$ is the Riemann Zeta function. By defining the electron-phonon coupling constant as $\Sigma = \frac{24\zeta(5)k_B^5\nu^2 m N(E_F)}{\pi c_l^2 k_F \hbar^6}$ the final expression then reads

$$
\dot{Q}_{\text{e-phn}} = \Sigma V (T_e^5 - T_{\text{phn}}^5).
\tag{5.15}
$$

Over the course of this derivation, a couple of assumptions about the system have been made implicitly [25].

- The phonon DOS that is used, $V/(2\pi)^3$ assumes a 3D bulk material.
- The relation for linear dispersion, $\omega_q = c_l q$, is only valid for acoustic phonons, which means that the model assumes low temperatures so that only low-energy, long-wavelength sounds are thermally populated.
- The coupling coefficient, $g_k = \nu\omega_q^{1/2}$ assumes that the electron phonon interaction can be treated as a scalar deformation potential, which means that only longitudinal phonons couple to electrons and that transverse phonons can be ignored.
- The system is assumed to be in the clean limit, i.e. that strict momentum conservation, $k' = k \pm q$, applies.

For a system where these assumptions are not valid, the temperature dependence for the heat flow might not be strictly T^5 and can for example instead be T^4 or T^6 depending on the regime [2].

5.2 Electron-photon coupling

Apart from the electron-phonon coupling, the electron photon coupling also contribute to the heat flow from the island. This heat flow is what was measured as thermal emission in the last chapter. To calculate the total power that leaves the island via electron-photon coupling we only need to integrate Eq. (4.14) over all frequencies.

$$\begin{aligned}
P_{\mathrm{JN}} &= |t(\omega)|^2 \int_0^\infty \frac{d\omega}{2\pi}\hbar\omega\left(\frac{1}{e^{\frac{\hbar\omega}{k_BT_R}}-1} - \frac{1}{e^{\frac{\hbar\omega}{k_BT_L}}-1}\right) \\
&= \frac{|t(\omega)|^2}{2\pi}\left(\int_0^\infty dx\frac{(k_BT_R)^2}{\hbar}\frac{x}{e^x-1} - \int_0^\infty dx\frac{(k_BT_L)^2}{\hbar}\frac{x}{e^x-1}\right) \\
&= \frac{|t(\omega)|^2}{2\pi}\frac{k_b^2}{\hbar}(T_R^2 - T_L^2)\frac{\pi^2}{6} = \frac{4RZ_0}{(R+Z_0)^2}\frac{k_B^2\pi^2}{6h}(T_e^2 - T_\gamma^2),
\end{aligned} \tag{5.16}$$

where we in the last step changed from angular frequency to bare frequency and used that $|t(\omega)|^2 = 4RZ_0/(R+Z_0)^2$, see Eq. (4.11). Here, T_γ denotes the radiation temperature, i.e. the photon temperature, while T_e is the electronic temperature of the island. The temperature T_L in Eq. (4.14) is therefore the temperature T_e of the copper island and T_R is the temperature present at the other end of the transmission line. This photonic heat conduction has been measured experimentally in [3, 4]. Due to the T^2 dependence of the electron-photon coupling, compared to T^5 for electron-phonon coupling, the electron photon coupling will be the dominating heat flow mechanism at low enough temperatures.

5.3 Heat flow in a superconductor

In a bulk superconductor at low temperatures, heat conduction is exponentially suppressed, and superconductors are therefore often used as thermal insulators. The Cooper pair condensate carries no entropy or heat, which means that it is only quasiparticles with energies above the superconducting gap Δ which will contribute to the heatflux in a superconductor [8]. This heat flow is typically negligible compared to for example the electron-phonon coupling in a normal metal structure, but if a normal metal is brought into contact with a superconductor, the inverse proximity effect will change the properties of the superconductor close to the interface, and the heat flow can increase considerably [27].

5.3.1 Quasiparticle heat flow

At low temperatures $T \ll T_c$, the number of quasiparticles in a superconductor without inverse proximity effect are exponentially small. BSC theory predicts the quasiparticle density n_{qp} to be [28]

$$n_{\mathrm{qp}} = D(E_F)\sqrt{2\pi k T_{\mathrm{qp}}\Delta}e^{-\Delta/kT_{\mathrm{qp}}}, \tag{5.17}$$

where $D(E_F)$ is the density of states at the Fermi energy in the normal state and T_{qp} is the quasiparticle temperature. However, experiments have shown larger quasi-particle densities than what is predicted by Eq. (5.17) [8], especially at the lowest temperature. Although the quasiparticle density have been shown to follow the exponential suppression $\propto e^{-\Delta/kT}$ down until 150 mK, n_{qp} saturates at lower temperatures [29]. These excess quasiparticles are most likely a result of high frequency noise radiated from the environment which can break Cooper pairs into two quasiparticles [8].

As the Cooper pair condensate carries no entropy or heat, it is only the quasiparticles that may contribute to electric heat flow and dissipation in a superconductor. If two quasiparticles of opposite momenta k and $-k$ recombine to form a Cooper pair, a phonon with energy 2Δ will be released. This heat dissipation mechanism we will refer to as quasiparticle-phonon coupling. In the limit $T_{\mathrm{phn}} \ll T_{\mathrm{qp}} \ll \Delta/k_B$ this heatflux can be calculated as [8]

$$P_{\text{qp-phn}} \approx 0.98e^{-\Delta/(k_B T_{\mathrm{qp}})}\Sigma V(T_{\mathrm{qp}}^5 - T_{\mathrm{phn}}^5). \tag{5.18}$$

This equation is essentially the prefactor $0.98e^{-\Delta/(k_B T_{\mathrm{qp}})}$ multiplied with the normal state heat flow described in Eq. (5.15). The exponential suppression of the heat flow was experimentally tested in Ref. [30].

5.3.2 Proximity and inverse proximity effect

If a normal metal is put into direct contact with a superconductor, some of the superconducting properties will leak into the normal metal (proximity effect) but some of the normal metal properties will also leak into the superconductor (inverse proximity effect).

The inverse proximity effect in a superconductor suppresses the superconducting gap Δ, and introduces subgap states within the gap. An electron approaching the NS interface from the normal metal side will survive as a subgap quasiparticle a distance L into the superconductor with a probability proportional to $e^{-L/\xi}$, where ξ is the superconducting coherence length [27]. The superconducting coherence length defines the length scale over which a superconductor recovers it's properties and is a fundamental length scale describing a superconductor [11]. This inverse proximity effect has been shown to significantly increase the heat conduction of the superconductor in leads up to around the distance ξ away from an ohmic contact to a normal metal [27].

5.4 Measured heat flow

To study the heat balance of the island, we assume a situation as the one illustrated in Fig. 5.1. The electrons of the copper island are heated to the temperature T_{NIS} through absorption of microwave photons originating from an ingoing microwave signal $P_{\mathrm{pht}}^{\mathrm{in}}$. Alongside this intentional signal, an environmental leakage heat flow P_{leak} also enters the system through the microwave line. This heat leak is the reason why the electronic saturation temperature of the island is 35 mK instead of the 10 mK base temperature of the dilution refrigerator. Because this saturation temperature was observed to change depending on the filtering used in the microwave line in Section 3.4.2, this indicates that P_{leak} enters the device through this channel. In the following analysis, this background heating is accounted for by setting the environment temperature $T_\gamma = 35$ mK and the phonon temperature $T_{\mathrm{phn}} = 35$ mK.

The heat flow out from the normal copper island occurs either via emission of a photon or by transferring energy to the phonons, contributing to the heat flows $P_{\mathrm{pht}}^{\mathrm{out}}$ and P_{phn} respectively. The temperature is probed using a current biased NIS junction with the current $I_{\mathrm{NIS}} = -20$ pA. This contributes with a heat flow $P_{\mathrm{NIS}}^{\mathrm{therm}}$, but since the current is small, this heat flow is assumed to be negligibly small in the following analysis. The island can also be heated using a current biased NIS junction. As was shown in Section 4.3.6, this heat flow is similar to the microwave heating $P_{\mathrm{pht}}^{\mathrm{in}}$. Therefore, we choose to only focus on the microwave heating in this chapter.

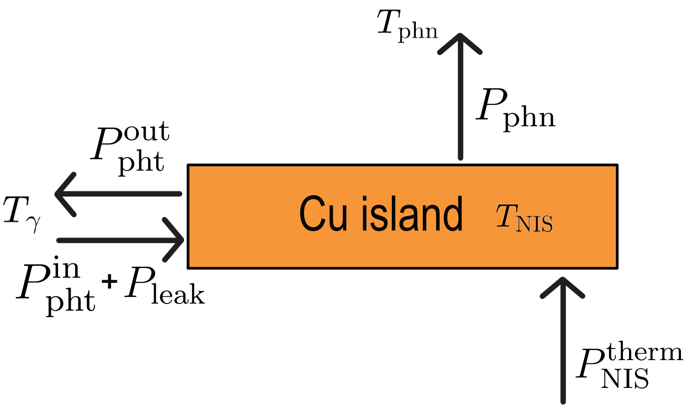

Figure 5.1: Illustration of the heat flows and temperatures related to the copper island. P_{phn} and $P_{\mathrm{pht}}^{\mathrm{out}}$ denotes the heat flow due to electron phonon and electron photon coupling, while $P_{\mathrm{pht}}^{\mathrm{in}}$ is the heating from the applied ingoing microwave signal. $P_{\mathrm{NIS}}^{\mathrm{therm}}$ is the small self-heating power that the current biased NIS junction working as a thermometer contributes with, while P_{leak} is a leakage heat flow.

5.4.1 Observation of enhanced outgoing heat flow

The microwave heating power, $P_{\text{pht}}^{\text{in}}$, required to elevate the copper island to a specific temperature T_{NIS} is shown in Fig. 5.2. We heated the island using several different frequencies, with the ingoing lines calibrated according to the procedure in Section 4.3.6. In the steady state, the heat flow out of the island must equal the power supplied to it, such that $P_{\text{out}} = P_{\text{in}}$. By assuming that the primary relaxation channels are electron-phonon and electron-photon coupling, the outgoing heat flow is:

$$P_{\text{out}}^{\text{model}} = P_{\text{pht}} + P_{\text{phn}} = \frac{4RZ_0}{(R+Z_0)^2}\frac{k_B^2\pi^2}{6h}(T_e^2 - T_\gamma^2) + \Sigma V(T_e^5 - T_{\text{phn}}^5). \tag{5.19}$$

For the modelling, we determine the copper island volume $V_{\text{island}} \approx 2.8 \cdot 10^{-20}$ m^3 by estimating the geometrical volume from the dimensions shown in Fig. 2.2. We also account for the two gold pads connecting the island to the aluminium lines, as they also contribute to electron-phonon relaxation. These have a combined volume of $V_{\text{pads}} \approx 5.4 \cdot 10^{-20}$ m^3. The material constants are taken as $\Sigma_{\text{Cu}} \approx 2{\cdot}10^9$ W/K^{5}m^3 and $\Sigma_{\text{Au}} \approx 2.4{\cdot}10^9$ W/K^{5}m^3 [2]. These values for the electron-phonon coupling constants, together with the T^5 dependence have been shown to be close to the measured electron-phonon heat flow in previous work [7, 18]. In Ref. [7] the electron phonon-coupling constant was measured to be $\Sigma_{\text{Cu}} = 3.7 \cdot 10^9$W/K^{6}m^3. In Ref. [18] the heat flow was instead measured in a structure consisting of both copper and gold, and the jointly measured coupling constant was found to be $\Sigma_{\text{Cu/Au}} = 2.5{\pm}0.1{\cdot}10^9$W/K^{5}m^3. This structure also had a similar geometrically estimated volume as the one investigated in this thesis.

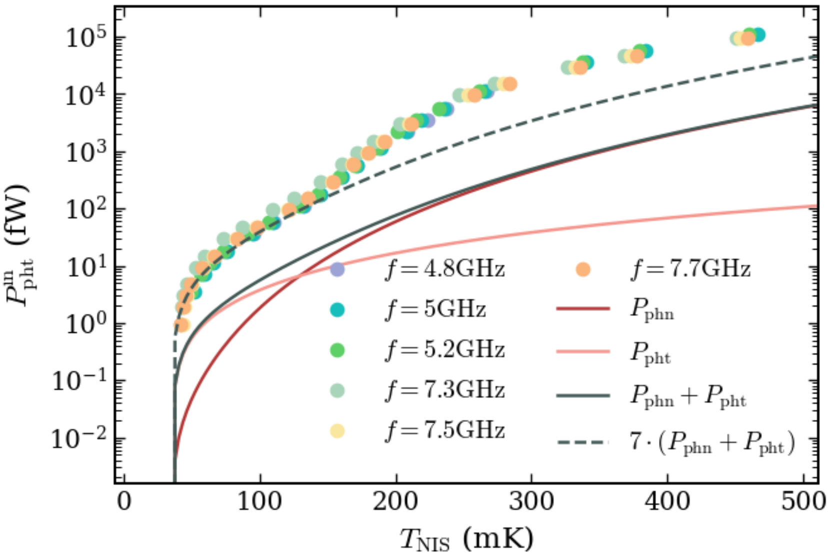

Figure 5.2: Heat flow $P_{\text{pht}}^{\text{in}}$ in from the copper island as a function of temperature T_{NIS}, using different frequencies for the microwave heating ($P_{\text{in}}^{\text{xGHz}}$). The ingoing line is calibrated as in Section 4.3.6. The solid lines show the different contributions of the outgoing heat flow in Eq. (5.19).

The predicted heat flow from Eq. (5.19) is plotted as a solid grey line in Fig. 5.2 alongside the measured data. As is evident from the figure, the heat flow predicted by the standard model is lower by at least an order of magnitude compared to the measured ingoing power $P_{\text{pht}}^{\text{in}}$. To explicitly quantify this difference, a dashed line showing the model scaled up by a factor of seven is included in the plot. This scaled model matches the data well at low temperatures, demonstrating that the enhanced heat flow is consistently seven times larger than the standard prediction below 130 mK. Above 150 mK, however, the discrepancy widens further as the required ingoing power begins to increase much more quickly with temperature than even the scaled model.

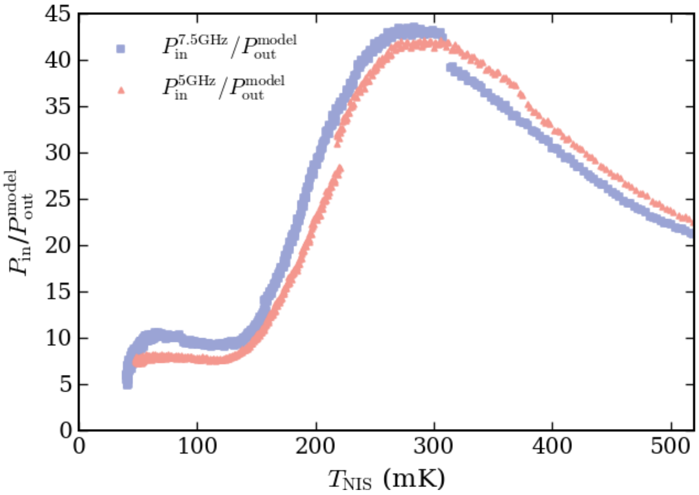

Figure 5.3: Ratio between the measured and modelled heat flow, i.e. how many times larger the measured heat flow is compared to the modelled one in Eq. (5.19). The ratio is shown both for the heat flow obtained with an ingoing microwave heating frequency of 5 and 7.5 GHz.

To better visualize how the presence of clean NS contacts and inverse proximity effect changes the temperature dependence of the device, Fig. 5.3 plots the ratio $P_{\text{in}}/P_{\text{out}}^{\text{model}}$. This ratio effectively quantifies how many times the actual heat flow exceeds the theoretical prediction allowing us to identify 2 distinct regions.

- **Low Temperature regime (50–130 mK):** The ratio $P_{\text{in}}/P_{\text{out}}^{\text{model}}$ remains roughly constant. This suggests that the measured heat flow shares the same temperature dependence as the model.

- **High temperature regime (>150 mK)** The ratio $P_{\text{in}}/P_{\text{out}}^{\text{model}}$ increases quickly from approximately 7 to almost 40. This indicates that the measured heat flow is far more sensitive to temperature than the model, increasing much faster than the predicted T^2 or T^5 scaling.

5.4.2 High-Temperature Regime: (> 150 mK)

To gain an understanding of what happens in the high-temperature regime, we plot the experimental data in Fig. 5.4 in the so-called Arrhenius plot. This is a useful tool to determine if the data follows a thermal activation dependence of the form $Ce^{-\Delta/(k_\mathrm{B}T)}$. We see that the previously curved data points of Fig. 5.2 form a straight line in the Arrhenius plot. This implies that in this regime, a thermal activation process takes place. With the data forming a straight line, we can quantitatively extract the activation energy Δ by performing a linear fit. By taking the logarithm of the applied power and fitting it against $1/T$, we obtain:

$$\log(P_\mathrm{in}) = \log\left(Ce^{-\Delta/(k_\mathrm{B}T)}\right) = -\frac{\Delta}{k_\mathrm{B}} \cdot \frac{1}{T} + \log C. \tag{5.20}$$

The fit is performed in the temperature range 160 mK $< T <$ 500 mK. The resulting fit for the 5 GHz signal yields an activation energy of $\Delta = 124$ μeV, while the 7.5 GHz signal yields $\Delta = 116$ μeV (Fig. 5.4).

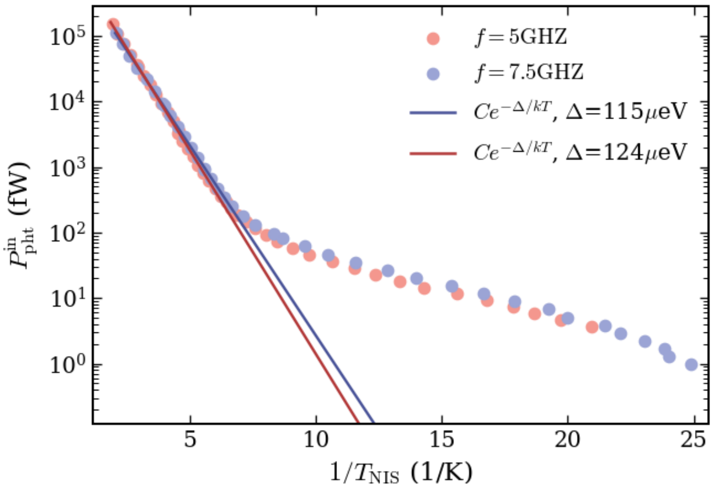

Figure 5.4: Fit of the function $e^{-\Delta/(k_\mathrm{B}T)}$ to the experimentally measured heat flow of the device, using an ingoing microwave signal of 5 GHz and 7.5 GHz, yielding $\Delta = 124$ μeV and $\Delta = 115$ μeV. The fit is performed in the temperature regime $160 < T < 500$ mK.

These extracted activation energies are comparable to the superconducting energy gap of aluminium, although somewhat lower. To put the extracted value into contect, the thin aluminium of the NIS junctions measured in Chapter 3 had a superconducting gap of $\Delta = 240$ μeV. However, the aluminium used for the clean NS contacts is thicker, which typically yields a bulk superconducting gap value of $\Delta = 180$ μeV [31]. Since our extracted activation energy (~ 120 μeV) is still distinctly lower than this bulk value, the further decrease must be attributed to the inverse proximity effect. This effect locally suppresses the superconducting gap close to the NS interface, lowering the energy barrier for quasiparticle excitation.

Consequently, because of this lowered barrier, heat begins to flow away via the superconducting aluminium leads in this high-temperature regime. As the density of thermally excited quasiparticles increases, the aluminium is no longer a good thermal insulator. As noted in previous works [27, 30], the exponential suppression become less effective as the temperature is increased. This aligns with our observation that thermally activated quasiparticles dominate the heat transport at elevated temperatures.

5.4.3 Low-Temperature Regime: (50–130 mK)

Although the low temperature regime follows the same dependence as the model, we still want to test if another power-law dependence could work. We assume a simple power-law model for the outgoing heat flow of the form $P_{\mathrm{out}} \approx C \cdot T^n$, where n is an integer. By taking the logarithm of the measured heating power P_{in} and performing a linear fit against $\log T$ we obtain

$$\log P_{\mathrm{in}} = \log(C \cdot T^n) = \log C + n \cdot \log T. \tag{5.21}$$

The linear slope will thus directly yield the temperature exponent n. The results of this power-law fit for both the 5 GHz and 7.5 GHz data are shown in Fig. 5.8. Between 50 and 130 mK, the data is described by an exponent of $n \approx 3$. A higher exponent, $n \geq 4$ or a lower one, $n \leq 2$, does not fit the data equally well. As the heat flow is 7 times higher than the T^3 dependence arising as a combination of electron-phonon and electron-photon coupling, see Fig. 5.2, the question is if both the electron-photon and electron-phonon coupling can be increased as a coincident by the same amount. This is what we address next.

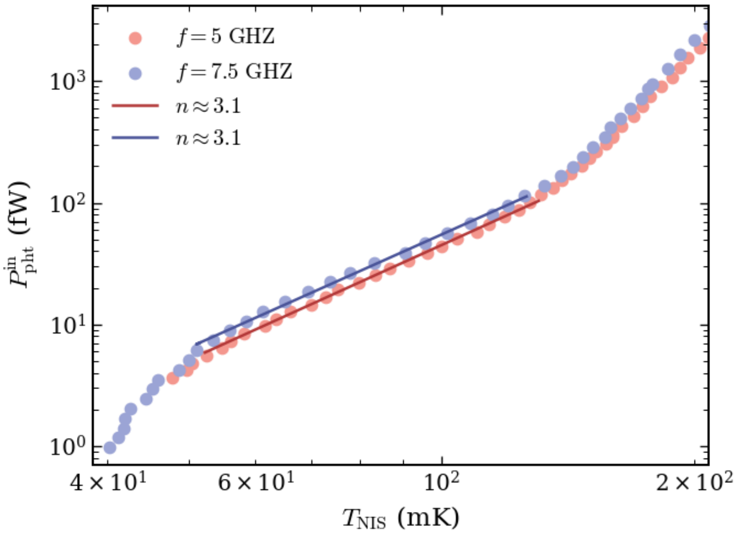

Figure 5.5: Fit of the power law $C \cdot T^n$, to the experimentally measured heat flow of the device, using an ingoing microwave signal of 5 GHz and 7.5 GHz.

The absorption measured in Fig. 4.3 shows that the photon absorption is close to unity. As the photon emission is the reverse process of the absorption, this supports that the photon emission and the corresponding photonic heat flow should be the quantum limited value of Eq. (5.16). This was further confirmed by the measurement of close to unity emission in Section 4.4. Therefore, it does not seem feasible that the photonic heat flow could be 7 times higher. The enhanced heat flow thus needs to be a result of electron-phonon coupling.

To estimate how much added heat flow the inverse proximity effect may contribute to, we make a rough estimate of the volume of the superconductor that is affected by the inverse proximity effect. If we assume the superconducting material that is within a coherence length $\xi \approx$ 150 nm [27] from the NS interface in Fig. 2.1b to contribute with close to normal state electron-phonon coupling, the resulting affected volume will be larger than the normal metal volume in Eq. (5.19). Although we have not directly measured the coherence length in our device, this estimate shows that the heat flow from the inverse proximity effect is non-negligible and need to be accounted for. Hence the inverse proximity enhanced heat flow seems to be justified.

The last item that remains to be understood is why the temperature dependence is still T^3 and not the one from electron-phonon coupling, which would yield T^5 for a standard normal metal as in Eq. (5.19). This T^3 dependence is a clear modification from the standard bulk electron-phonon scaling of T^5 used in Eq. (5.15). However, also the T^3 dependence can be motivated through the inverse proximity effect. As described in Section 5.3, the electron-phonon coupling in a superconductor is exponentially suppressed with $e^{-\Delta/(k_B T)}$. In a superconductor affected by the inverse proximity effect, the proximitized gap will be continuously varying from 0 at the interface until the full superconducting gap is recovered at a length much larger than ξ from the interface. The resulting heat flow will thus be a mix of thermal activation over the different gap values and hence likely yield a different temperature dependence than exponential or the T^5. Thus the T^3 may likely arise from proximity influenced temperature dependence that coincidentally match the one predicted by the initial modelling.

5.4.4 Comparison to previous experiments

The measured outgoing heat flow from our device is significantly larger than both standard theoretical predictions and results reported in previous works on similar structures. In fact, several previous works [7, 18, 32] have reported electron-phonon and heat flows in line with P_{pht}, plotted as a red line in Fig. 5.2. A main structural difference between our device and those measured in Ref. [7, 18, 32] is the presence of clean NS contacts in our device. This introduces the inverse proximity effect into the superconducting leads, which is likely to increase the heat conduction as discussed in Section 5.3.2.

Another comparison point is the experiments on photonic heat conductance in Ref. [3, 4]. In these devices, direct NS contacts were present. They found the thermal transport to be well described by models based on the quantized photonic heat flow combined with the usual, non-increased, electron-phonon heat flow. However, the heat flows in those experiments were not really measured directly. Because they relied on fitting their thermal models to temperature data, there might be some wiggle room for the electron-phonon coupling constant or volume in the modelling. It is therefore unclear how their results would be affected if the actual heat flow were significantly larger, as is seen for our device.

Additionally, there is also a clear structural difference between our device and those measured in Ref. [3, 4], namely that the normal metal of our device connects to superconducting pads of a large area (shown in Fig. 2.1a). In contrast, the superconducting metal in [3, 4] consists of narrow leads with widths similar to the normal metal. The inverse proximity effect typically decays over the superconducting coherence length, ξ. In our geometry, the large lead area means that a significantly larger volume of the aluminium lead is affected by the inverse proximity effect compared to the narrow-lead designs used in previous works, and hence is a likely reason for the increased heat flow. This creates a larger volume of superconducting metal with an increased density of quasiparticles which can contribute to the thermal transport.

5.5 Improvements for future devices

To improve thermal isolation in future devices, the heat flows arising from the inverse proximity effect needs to be eliminated. One way of doing this would be to fabricate a device with narrower superconducting leads. This would directly decrease the physical volume affected by the inverse proximity effect, thus yielding a smaller heat flow and a device more similar to the ones measured in [3, 4]. By creating superconducting leads with a width of 100 nm instead of the wide leads used in this device, the volume affected by the inverse proximity effect would be reduced by an order of magnitude. As a result, the excess heat flow should also be suppressed by an order of magnitude.

Another option would be to fabricate a similar device to the one in this thesis but using a different superconductor with a higher critical temperature T_c. A higher T_c provides a larger superconducting gap, which suppresses both the inverse proximity effect, by having shorter length scale ξ, and the thermal activation of quasiparticles, since the probability scales inversely with the gap Δ. A common candidate for this type of experiment would be niobium. The superconducting gap of niobium is about an order of magnitude larger than aluminium [33], which should result in a coherence length that is around 3 times smaller [27]. Thus the volume and heat flow is predicted to be reduced by almost two orders of magnitude, rendering the excess heat flow resulting from the inverse proximity effect negligible.

By fabricating a device with better thermal isolation, ensuring a heat flow governed by Eq. (5.19), it should be possible to achieve a device with a dominating photonic heat flow at low temperatures. With the normal metal island heated to, for example, 50 mK, such a device should exhibit a photonic heat flow an order of magnitude larger than the heat flow originating from electron-phonon coupling, assuming an environment temperature of $T_\gamma = 35$ mK. Such an experimental regime has so far not been shown, making the realization of a device where thermal dissipation is strictly dominated by electron-photon coupling a goal for future work.

Chapter 6

Conclusion and outlook

In this thesis, we have studied thermal emission and absorption of microwave photons. A copper island has served the role of a resistor and a variable thermal bath, which we have been able to heat either by sending in a microwave signal that gets absorbed by the island, or by applying a voltage bias over one of the NIS junctions. The electronic temperature of the island has then be probed through use of a current biased NIS junction. A superconducting aluminium lead, connecting to the island via a clean NS contact, were used to send in and emit microwave photons. We found that we can achieve and measure close to unity absorption and emission with the device.

Being able to perform accurate thermometry of the electronic temperature of the copper island provides the foundation for the emission and absorption measurements presented in this thesis. In Chapter 3, a current biased NIS junction was proved to provide such precise temperature readings. By varying the bath temperature of the cryostat we showed that the junction works as a thermometer in the temperature range $35-500$ mK, which is therefore the temperature range within which the measurements of this thesis is performed. Furthermore, the $I-V$ characteristics of the NIS junction was measured when the island was heated with an ingoing microwave signal, and it was shown that the temperature readings indeed is the result of a thermal response.

Measurements of the thermal emission from the device demonstrate near-unity emission efficiency, within an experimental uncertainty of approximately 50%. The theoretical unity emission is predicted to follow quantum limited Johnson-Nyquist noise. Because the absorption efficiency is close to unity, the experimental accuracy is limited by the line calibration rather than the device itself. The emission measurements demonstrate the successful realization of a thermal photoemitter, as well as providing a direct measurement of the photonic heat flow.

The heat flow out from the normal metal island was shown to be enhanced compared to what is predicted by assuming the electron-phonon and electron-photon coupling to be the dominating heat dissipation mechanisms, and using a typical value for the electron-phonon coupling constant Σ. Furthermore, the measured heat flow in this thesis exceeds what has been measured previously in other works studying similar devices. This enhancement is likely caused by the geometrical differences between our device and those in previous works, most importantly the clean NS contacts and the larger area of the superconducting leads. Our interpretation is that these contacts introduces inverse proximity effect, which expands the effective volume for electron-phonon coupling at low temperatures, and leads to a thermally activated quasiparticle heat flow at higher temperatures.

As a result of the thesis work, we propose the following improvements to future devices to reduce the enhanced heat flow and achieve proper thermal isolation. A device with narrower superconducting leads would decrease the volume affected by the inverse proximity effect, and should thus yield a smaller heat flow more similar to the devices measured in previous works. Additionally, a similar device as the one used in this thesis, but using niobium instead of aluminium as a superconductor would also improve thermal isolation. The larger superconducting gap Δ of niobium suppresses the inverse proximity effect and the thermal activation of quasiparticles, thereby eliminating these channels for thermal transport. Such a device should be able to reach a regime where the heat dissipation is dominated by electron-photon coupling.

Lastly, an interesting aspect that has not been considered much in this thesis is bolometry and sensitivity. The near to unity absorption efficiency of the device provides an excellent foundation for it to work as a sensitive bolometer over a wide bandwidth, capable of detecting small amounts of radiation. However, to increase the sensitivity of the device, it would be beneficial if the enhanced heat flow of the device that is currently seen could be suppressed.

In summary, we have in this thesis shown that we are able to achieve close to unity absorption and thermal emission with the device, thus providing a direct measurement of quantum limited photonic heat conduction. The device shows great potential to work as a thermal photon source or sensitive bolometer.

Bibliography

[1] C. Gerry and P. Knight, *Introductory quantum optics* (Cambridge University Press, Cambridge, 2004).

[2] F. Giazotto, T. T. Heikkilä, A. Luukanen, A. M. Savin, and J. P. Pekola, "Opportunities for mesoscopics in thermometry and refrigeration: physics and applications", Rev. Mod. Phys. **78**, 217–274 (2006).

[3] M. Meschke, W. Guichard, and J. P. Pekola, "Single-mode heat conduction by photons", Nature **444**, 187–190 (2006).

[4] M. Partanen, K. Y. Tan, J. Govenius, R. E. Lake, M. K. Mäkelä, T. Tanttu, and M. Möttönen, "Quantum-limited heat conduction over macroscopic distances", Nature Physics **12**, 460–464 (2016).

[5] H. Nyquist, "Thermal agitation of electric charge in conductors", Phys. Rev. **32**, 110–113 (1928).

[6] P. Krantz, M. Kjaergaard, F. Yan, T. P. Orlando, S. Gustavsson, and W. D. Oliver, "A quantum engineer's guide to superconducting qubits", Applied Physics Reviews **6**, 021318 (2019).

[7] M. Nahum and J. M. Martinis, "Ultrasensitive-hot-electron microbolometer", Applied Physics Letters **63**, 3075–3077 (1993).

[8] J. T. Muhonen, M. Meschke, and J. P. Pekola, "Micrometre-scale refrigerators", Reports on Progress in Physics **75**, 046501 (2012).

[9] H. B. Callen and T. A. Welton, "Irreversibility and generalized noise", Phys. Rev. **83**, 34–40 (1951).

[10] D. M. Pozar, *Microwave engineering*, 4th ed. (Wiley, 2021).

[11] J. F. Annett, *Superconductivity, superfluids, and condensates* (Oxford University Press, Mar. 2004).

[12] J. Bardeen, L. N. Cooper, and J. R. Schrieffer, "Theory of superconductivity", Phys. Rev. **108**, 1175–1204 (1957).

[13] V. F. Maisi, "Andreev tunneling and quasiparticle excitations in mesoscopic normal metal - superconductor structures: dissertation", PhD thesis (Aalto University, Finland, 2014).

[14] Y. Imry, *Introduction to mesoscopic physics*, 2nd ed. (Oxford University Press, 2001).

[15] R. C. Dynes, V. Narayanamurti, and J. P. Garno, "Direct measurement of quasiparticle-lifetime broadening in a strong-coupled superconductor", Phys. Rev. Lett. **41**, 1509–1512 (1978).

[16] J. P. Pekola, V. F. Maisi, S. Kafanov, N. Chekurov, A. Kemppinen, Y. A. Pashkin, O.-P. Saira, M. Möttönen, and J. S. Tsai, "Environment-assisted tunneling as an origin of the Dynes density of states", Phys. Rev. Lett. **105**, 026803 (2010).

[17] A. V. Feshchenko, L. Casparis, I. M. Khaymovich, D. Maradan, O.-P. Saira, M. Palma, M. Meschke, J. P. Pekola, and D. M. Zumbühl, "Tunnel-junction thermometry down to millikelvin temperatures", Phys. Rev. Appl. **4**, 034001 (2015).

[18] D. Majidi, M. Josefsson, M. Kumar, M. Leijnse, L. Samuelson, H. Courtois, C. B. Winkelmann, and V. F. Maisi, "Quantum confinement suppressing electronic heat flow below the wiedemann–franz law", Nano Letters **22**, PMID: 35030004, 630–635 (2022).

[19] C. D. Satrya, Y.-C. Chang, A. S. Strelnikov, R. Upadhyay, I. K. Mäkinen, J. T. Peltonen, B. Karimi, and J. P. Pekola, "Thermal spectrometer for superconducting circuits", Nature Communications **16**, 4435 (2025).

[20] C. D. Satrya, A. S. Strelnikov, L. Magazzù, Y.-C. Chang, R. Upadhyay, J. T. Peltonen, B. Karimi, and J. P. Pekola, *Heat measurement of quantum interference*, (2025) `https://arxiv.org/abs/2510.23092`.

[21] U. Vool and M. Devoret, "Introduction to quantum electromagnetic circuits", International Journal of Circuit Theory and Applications **45**, 897–934 (2017).

[22] B. Yurke and J. S. Denker, "Quantum network theory", Phys. Rev. A **29**, 1419–1437 (1984).

[23] G. Lindgren, H. Rootzén, and M. Sandsten, *Stationary stochastic processes for scientists and engineers*, 1st ed. (Chapman and Hall/CRC, 2013).

[24] E. André and D. Hermelin, "Microwave photon absorption and emission with a high impedance resonator-dqd device", Student Paper (2025).

[25] F. C. Wellstood, C. Urbina, and J. Clarke, "Hot-electron effects in metals", Phys. Rev. B **49**, 5942–5955 (1994).

[26] V. F. Maisi, S. V. Lotkhov, A. Kemppinen, A. Heimes, J. T. Muhonen, and J. P. Pekola, "Excitation of single quasiparticles in a small superconducting Al island connected to normal-metal leads by tunnel junctions", Phys. Rev. Lett. **111**, 147001 (2013).

[27] J. T. Peltonen, P. Virtanen, M. Meschke, J. V. Koski, T. T. Heikkilä, and J. P. Pekola, "Thermal conductance by the inverse proximity effect in a superconductor", Phys. Rev. Lett. **105**, 097004 (2010).

[28] J. P. Pekola, O.-P. Saira, V. F. Maisi, A. Kemppinen, M. Möttönen, Y. A. Pashkin, and D. V. Averin, "Single-electron current sources: toward a refined definition of the ampere", Rev. Mod. Phys. **85**, 1421–1472 (2013).

[29] P. J. de Visser, J. J. A. Baselmans, P. Diener, S. J. C. Yates, A. Endo, and T. M. Klapwijk, "Number fluctuations of sparse quasiparticles in a superconductor", Phys. Rev. Lett. **106**, 167004 (2011).

[30] A. V. Timofeev, C. P. García, N. B. Kopnin, A. M. Savin, M. Meschke, F. Giazotto, and J. P. Pekola, "Recombination-limited energy relaxation in a Bardeen-Cooper-Schrieffer superconductor", Phys. Rev. Lett. **102**, 017003 (2009).

[31] G. Marchegiani, L. Amico, and G. Catelani, "Quasiparticles in superconducting qubits with asymmetric junctions", PRX Quantum **3**, `10.1103/PRXQuantum.3.040338` (2022).

[32] J. T. Karvonen, L. J. Taskinen, and I. J. Maasilta, "Observation of disorder-induced weakening of electron-phonon interaction in thin noble-metal films", Phys. Rev. B **72**, 012302 (2005).

[33] A.-M. Valente-Feliciano, "Superconducting rf materials other than bulk niobium: a review", Superconductor Science and Technology **29**, 113002 (2016).

Appendix A

Tabulated attenuation

This appendix presents the complete list of the tabulated component gain along the ingoing and outgoing microwave lines at 5 and 7.5 GHz. Components for which no gain specifications could be found are denoted with "*". The gain has then be assumed to be the same as that of a similar component. Components where a linear interpolation (in dB) for both temperature and frequency were used to obtain the gain value are denoted "**".

Table A.1: Attenuation on Ingoing Line at 5 GHz

Type of Component	**Name**	**Gain (dB)**
Cable	141-36 SM+	-0.9
Splitter	ZX10R	-6.73
2 × Attenuator	FW-3+	2 × (-3.35)
Cable att. to rack	CBL-2MSMSM+	-1.87
Cable rack to cryostat	141-36SM+	-0.9
Cryostat attenuators		-59
Cryostat lines RT-4K**	0.86mm SCuNi-CuNi, 625 mm length	-2.7
Cryostat lines 4K-MXC**	0.86mm SCuNi-CuNi, 725 mm length	-3.18
Cable	086-6SM+	-0.27
Circulator	LNF-ISISC4-8A	-0.2
Cable	086-6SM+	-0.27
Cable*	BlueFors Cu	-0.52
Cable	PE3W05577-33CM	-0.52
Total		**-83.76**

Table A.2: Attenuation on Ingoing Line at 7.5 GHz

Type of Component	**Name**	**Gain (dB)**
Cable	141-36 SM+	-1.15
Splitter	ZX10R	-7.45
2 × Attenuator	FW-3+	2 × (-3.47)
Cable att. to rack	CBL-2MSMSM+	-2.36
Cable rack to cryostat	141-36SM+	-1.15
Cryostat attenuators		-59
Cryostat lines RT-4K**	0.86mm SCuNi-CuNi, 625 mm length	-3.6
Cryostat lines 4K-MXC**	0.86mm SCuNi-CuNi, 725 mm length	-4.27
Cable	086-6SM+	-0.36
Circulator	LNF-ISISC4-8A	-0.2
Cable	086-6SM+	-0.36
Cable*	BlueFors Cu	-0.69
Cable	PE3W05577-33CM	-0.69
Total		**-88.22**

Table A.3: Attenuation and Gain of Outgoing Line at 5 GHz

Type of Component	**Name**	**Gain (dB)**
Attenuation before first amplifier		
Cable att. before LNA*		-1.31
Circulator		-0.2
Filter	VHF-3100	-0.48
Filter	VLF-8400	-0.7
Gain/attenuation from amplifier and onwards		
Low noise amplifier (LNA)		+39
Cryostat attenuators		-4
Cryostat line RT-4K**	0.86mm SCuNi-CuNi, 625 mm	-2.7
Cable top of cryostat	141-12SM+	-0.32
3 × Amplifiers	ZX60	+3 × 20.89
3 × Attenuators	FW-3A	-3 × 3.35
Cable amplifier-rack	141-36SM+	-0.9
Cable rack-mixer	CBL-2MSMSM+	-1.87
Mixer	ZMX-10G	-5.3
Gain/attenuation after mixer: 50 MHz		
Attenuator	FW-3A	-2.9
Filter	VLF-3400	-0.01
Filter	VLF-80	-0.3
Amplifier	FEMTO	+20
Filter	VLF-80	-0.3
Total	**Before LNA + After**	**-2.69 + 95.02 (= 92.33)**

Table A.4: Attenuation and Gain of Outgoing Line at 7.5 GHz

Type of Component	**Name**	**Gain (dB)**
Attenuation before first amplifier		
Cables att. before LNA*		-1.74
Circulator	how many?	-0.2
Filter	VHF-3100	-0.6
Filter	VLF-8400	-1
Gain/attenuation from amplifier and onwards		
Low noise amplifier (LNA)		+41
Cryostat attenuators		-4
Cryostat line RT-4K**	0.86mm SCuNi-CuNi, 625 mm	-3.6
Cable top of cryostat	141-12SM+	-0.45
3 × Amplifiers	ZX60	+3 × 20.97
3 × Attenuators	FW-3A	-3 × 3.47
Cable amplifier-rack	141-36SM+	-1.15
Cable rack-mixer	CBL-2MSMSM+	-2.36
Mixer	ZMX-10G	-7.2
Gain/attenuation after mixer: 12.5 MHz		
Attenuator	FW-3A	-2.9
Filter	VLF-3400	-0.01
Filter	VLF-80	-0.3
Amplifier	FEMTO	+20
Filter	VLF-80	-0.3
Total	**Before LNA + After**	**-3.54 + 91.22 (= 87.68)**